ELSEVIER

Contents lists available at ScienceDirect

Geochimica et Cosmochimica Acta

journal homepage: www.elsevier.com/locate/gca





Uranium oxidation states in zircon and other accessory phases

Shane K. Houchin ^{a,*}, François L.H. Tissot ^a, Mauricio Ibañez-Mejia ^b, Matthew Newville ^c, Antonio Lanzirotti ^c, Frank Pavia ^a, George Rossman ^d

- ^a The Isotoparium, Division of Geological & Planetary Sciences, Caltech, Pasadena, CA, USA
- ^b Department of Geosciences, Univ. of Arizona, Tucson, AZ, USA
- ^c Center for Advanced Radiation Sources, The University of Chicago, Chicago, IL, USA
- d Division of Geological & Planetary Sciences, Caltech, Pasadena, CA, USA

ARTICLE INFO

Associate editor: Georges Calas

Keywords: Uranium Zircon Oxygen fugacity XANES Oxybarometer

ABSTRACT

Zircon and other U-bearing accessory phases are important time-capsules for studying the evolution of Earth and other planetary bodies as these minerals can record both temporal and compositional information regarding their host rocks. In silicate melts, uranium can occur in either the U^{IV} , U^V , or U^{VI} valence state and its redox sensitive nature could, in principle, allow for information on magma oxygen fugacity (fO_2) to be gleaned from U-bearing phases provided they can incorporate multivalent U during crystallization. Currently, however, little is known regarding the details of how U is speciated in these minerals.

In this study, we conducted conventional X-ray absorption near-edge structure (XANES) spectroscopy at the U M_4 -edge on a set of natural zircon (n = 140), titanite (n = 9), apatite (n = 7), baddeleyite (n = 7), and garnet (n = 2) samples to determine the oxidation state of U in these crystals. We also collected U L_3 -edge spectra for select zircon samples to investigate the bonding environment of U using extended X-ray absorption fine structure (EXAFS) analysis. The effects of crystallographic orientation and radiation damage on zircon U M_4 -edge spectra are found to be minimal compared to the magnitude of the peak shifts associated with U oxidation state. We find that titanite and garnet contain only tetravalent U, while zircon, apatite, and baddeleyite can contain U of variable valence. Of these phases, zircon shows the greatest variability, with white-line energy, E_{wl} (i.e., peak absorbance) covering a range of >2.0 eV between grains: i.e., the entire energy range expected between pure U^{IV} and pure U^{VI} species. Moreover, a correlation is observed between the E_{wl} of zircon U M_4 -edge spectra (i.e., relative proportions of U^{IV} , U^{V} , U^{VI}) and the fO_2 of their host rocks. Our results thus establish U oxidation states in zircon as a powerful new tracer of magma redox. Since XANES is non-destructive and can be performed in situ, this technique can be utilized alongside other microanalytical methods (e.g., LA-ICPMS, SIMS) to further expand the breadth of information that can be extracted from single mineral grains.

1. Introduction

Zircon and other uranium bearing accessory phases (e.g., titanite, apatite, baddeleyite) are key materials for investigating the evolution of Earth's crust as they can be both precisely dated and contain unique geochemical information reflective of the environment in which they formed (Hanchar and Hoskin, 2003). Zircon grains, in particular, can be extraordinarily long-lived and can retain their original composition through weathering, diagenesis, and metamorphism on protracted, billion-year timescales (Harrison et al., 2017). This durability has resulted in the zircon record being one of the most complete archives of Earth's history. While many methods of interrogating these minerals

exist (e.g., U-Pb, O isotopes, and Lu-Hf in zircon), continued development of new tools to study these time capsules is a worthy effort that will provide valuable new insights into Earth's evolution.

One parameter of crustal magmas that has been elusive to constrain is oxygen fugacity (fO_2). This thermodynamic quantity controls the potential for redox-sensitive elements (e.g., iron, vanadium, uranium, or cerium) to occur in more oxidized or reduced states, and it is often the dominant control on the proportions of their different valence states present within a rock or mineral. In the context of igneous petrology, fO_2 serves as a measure of magma oxidation state and has a direct influence on the compositional evolution of the crystallizing phases and residual liquids. For example, high fO_2 magmas will tend to follow a

E-mail address: shouchin@caltech.edu (S.K. Houchin).

^{*} Corresponding author.

calc-alkaline differentiation trend while low fO_2 magmas follow a tholeiitic trend (e.g., Osborn, 1959; Richards, 2015; Cottrell et al., 2021). Current zircon-based oxybarometers, however, can be unreliable due to their dependence on element concentrations and compositional assumptions, which in practicality are often difficult to constrain (e.g., Trail et al., 2011; Smythe and Brenan, 2016). Given the importance of the U-Pb zircon geochronometer for dating magmatic crystallization, developing a technique that provides the ability to constrain magma redox conditions at the time of equilibration from the same crystals being dated would provide a valuable tool for studying crustal evolution on both long and short timescales.

Though typically considered in the context of geochronology, uranium (U) in zircon has several qualities which make it a promising system for use as a tracer of fO2. First, uranium is a redox sensitive element with three oxidation states (U^{IV}, U^V, U^{VI}). Second, although U in zircon is often assumed to be tetravalent (e.g., Cherniak et al., 1997), previous work has shown that zircon can contain appreciable amounts of multivalent U (Vance and Mackey, 1974; Farges and Calas, 1991; Farges et al., 1992; Zhang et al., 2003; Burnham and Berry, 2012; Tanaka and Takahashi, 2019). Third, the redox potentials of the $U^{IV} \rightleftharpoons U^{V}$ and $U^{V} \rightleftharpoons$ U^{VI} reactions in silicate melts lie on either side of the $Fe^{II} \Rightarrow Fe^{III}$ reaction (Schreiber, 1987), implying that uranium should be more sensitive to magma redox states than iron. Fourth, zircon incorporates U at high concentrations (100s-1000s of ppm) (Hanchar and Hoskin, 2003), enabling spectroscopic investigations of U speciation. And finally, at the fO2 values relevant to crustal magmas, oxidized U is expected to represent a significant proportion of the total U in the melt (up to 50 % at the Fayalite-Magnetite-Quartz (FMQ) buffer) (Halse, 2014). Given the characteristics listed above, the oxidation state of U in zircon has the potential to be developed into a tracer of magma oxygen fugacity if its valence can be accurately determined.

X-ray absorption spectroscopy (XAS) has proven to be a powerful tool for investigating element oxidation states, as it provides quantitative information on the electronic structure of specific elements within a material. This technique has been used with great success on several redox sensitive elements (e.g., Fe: Kelley and Cottrell, 2009; Berry et al., 2010; Brounce et al., 2015; V: Sutton et al., 2005; Ce: Trail et al., 2015), but to date, few studies have used XAS to investigate U in zircon (L₃-edge: Farges and Calas, 1991; L₃- and M₅-edge Tanaka and Takahashi, 2019). While these pioneering studies confirmed that zircon can contain oxidized U, they both analyzed a limited number of samples and were primarily focused on metamict zircon grains.

In this study, we investigate the oxidization state of uranium in a large set of natural U-bearing minerals (including zircon, titanite, apatite, baddeleyite, and garnet) using conventional U M_4 -edge X-ray absorption near edge structure (XANES) spectroscopy. For zircon from select localities, the bonding environment of U in these crystals was also studied using extended X-ray absorption fine structure (EXAFS) analysis (U L_3 -edge). Through careful consideration of the impact of potential systematic biases and confounding factors, such as crystallographic orientation and radiation damage, we show that XAS can provide an accurate and consistent measure of U oxidation states in zircon and other U-bearing minerals. Importantly, our data reveal that the energy of peak absorbance in U M_4 -edge zircon spectra correlates with the fO_2 of their host rocks. We discuss how these results open the door for XANES analysis of U in zircon to be used as a probe of magma oxygen fugacity.

2. Samples and methods

2.1. Samples

Mineral samples for this study were selected to cover a range of magma compositions, oxygen fugacities, ages, and tectonic environments. Several samples are also common reference materials and/or

contain multiple coexisting U-bearing accessory phases (e.g., FC-1 Duluth Gabbro, Fish Canyon Tuff). The majority of the minerals analyzed are from igneous rocks, although some of the titanite, garnet and baddeleyite grains analyzed are from metamorphic sequences (see Table 1). For zircon, baddeleyite, titanite, and apatite from reference localities (e.g., FC-1, FCT, Ecstall, Phalaborwa) mineral separation and mounts were made at the Arizona LaserChron Center at University of Arizona. New zircon samples prepared for this study were processed at Caltech (Harney Peak, Sturgeon Lake, Lassen, Long Valley, Pacoima Pegmatite) and the Arizona LaserChron Center (Bishop Tuff). All grains analyzed in this study were concentrated using standard mineral separation techniques (i.e., magnetic and heavy liquid separation). Mineral separates were hand-picked under a binocular microscope and mounted in 1-inch epoxy rounds. The average thickness of the mineral grains investigated is \sim 50–150 μm . Due to APS safety regulations for actinide research, epoxy sample mounts were encapsulated in 1 mil Kapton film. For samples that had undergone previous LA-ICPMS analyses, a subset of grains were chosen such that a representative sampling of other relevant quantities of the larger data set (i.e., U-Pb age, trace element concentrations) were covered. For samples with no pre-existing data for individual grains, crystals with the fewest number of cracks and inclusions were selected for analysis from each sample mount. In total, 140 individual zircon grains from 34 different rock samples were analyzed in this study, as well as 9 titanite from 3 samples, 7 apatite from 4 samples, 7 baddeleyite from 4 samples, and 2 garnet from 2 samples. Table 1 gives a complete list of the samples analyzed, along with their ages and host lithology.

2.2. SEM imaging

Backscattered electron (BSE) and cathodoluminescence (CL) images of all mineral grains measured in this study were collected prior to XAS analyses. Images were collected using a Zeiss 1550VP FE-SEM at the GPS Division Analytical Facility (Caltech) at an accelerating voltage of 20 keV. These images were used to identify areas of interest and avoid cracks, inclusions, or other imperfections on the grain surfaces. For grains having undergone LA-ICPMS prior to this study, these images allowed positioning of spots for XAS measurements in the same growth region as previous analyses.

2.3. μXRF mapping

X-ray fluorescence mapping of each grain was conducted at the Advanced Photon Source (APS, Argonne National Laboratory) Beamline 13-ID-E prior to XAS analyses. These maps were used to select the location of XAS analyses spots and to avoid subsurface inclusions that were not apparent in BSE or CL images (Fig. 1). Maps were collected using a monochromatic incident X-ray beam focused to 2×2 microns using silicon mirrors (Rh-coated) in a Kirkpatrick-Baez (KB) geometry (Sutton et al., 2017). Fluorescence counts were measured using a sevenelement, silicon-drift-diode detector array (SX7, Canberra) with pulseprocessing provided by an Xspress 3 digital X-ray processor system (Quantum Detectors). For mapping, an incident beam energy of 17.5 keV was used with an incident flux of $\sim 6.75 \times 10^{11}$ photons/sec. For zircon and baddeleyite samples, false-color RGB images of Ti $K\alpha$, U $L\alpha$, and Ca $K\alpha$ emission intensities were used to select the location of analysis spots and to avoid inclusions, as Ca and Ti tend to have high concentrations in minerals that often occur as zircon inclusions (e.g., apatite, rutile, rock-forming minerals). In some instances, grains were mapped using an incident beam energy closer to the U M₄-edge (3.76 keV with an incident flux of $\sim 3.5 \times 10^{11}$ photons/sec) and the U M β emission intensity was visualized instead of U La. Similarly, RGB maps of Ti $K\alpha$, U $L\alpha$, K $K\alpha$ and Hf $L\alpha$, U $L\alpha$, K $K\alpha$ were used to select analysis locations for apatite and titanite, respectively. It should be noted that

Table 1
List of samples analyzed in this study along with their host lithology, age, and the analyzed phases.

Sample	Lithology	Age (Ma)	Phases (n = # grains)	Ref.
Volcanics				
Lassen (LF042-02)	rhyodacite	0.035	zircon (n = 4)	1
Long Valley (MC18-02,04)	pumice/ rhyolite	0.1-0.16	zircon (n = 5)	2
Bishop Tuff (BT)	ignimbrite	0.76	zircon (n = 6)	3,4
Fish Canyon Tuff (FCT)	dacite	28.4	zircon (n = 15), titanite (n = 4), apatite (n = 4)	5
Arcs				
Sierra Nevada Plutons				
Mt. Whitney granite (W-35)	granite	85.3	zircon (n = 1)	6,7
Paradise granodiorite (KC-17,-19)	granodiorite	87	zircon (n = 4)	6,7
Lone Pine granodiorite (LP-9)	granodiorite	89.8	zircon (n = 2)	6,7
Dragon pluton (Dragon1)	granodiorite	102	zircon (n = 3)	6,7
Bullfrog pluton (14BF-2, 3)	granite	102.3	zircon (n = 3)	6,7
Independence pluton (11SN15,31)	granite	100.5-104	zircon (n = 4)	6,7
Hidden Lakes Mafic Complex	3			
HL-17-02	anorthosite	95.7	zircon (n = 4)	8
SNB-14-40	cumulate monzonite	90.5	zircon $(n = 7)$	8
SNB-14-34	liquid-like monzodiorite	96.5	zircon (n = 4)	8
SNB-16-12	liquid-like monzodiorite	90.5	zircon $(n = 5)$	8
SNB-16-6	liquid-like monzodiorite	95.1	zircon (n = 3)	8
SNB-16-9	liquid-like monzonite	95.6	zircon (n = 4)	8
Dariv Igneous Complex	aqua inte monuonite	30.0	in the state of th	Ü
MO-11-12	monzogabbro	502	zircon (n = 4)	9
MO-11-14	monzodiorite	502	zircon $(n = 4)$	9
MO-11-14 MO-11-16	felsic dike	502	zircon (n = 5)	9
MO-11-19	lamprophyre dike	502	zircon (n = 5)	9
MO-11-26	quartz monzonite	502	zircon (n = 3) $zircon (n = 4)$	9
MO-11-23	monzonite	502	zircon $(n = 4)$	9
Ecstall Pluton	granodiorite	91.5	zircon (n = 5), titanite (n = 3)	10
Temora II	diorite	416.8	zircon (n = 2)	11
SPGs	tion tie	410.0	2ncon (n-2)	11
Harney Peak (HP44A, HP21C)	granite	1700	zircon (n = 8)	12,13
Sturgeon Lake (SP-16-52)	granite	2671	zircon (n = 5)	12,10
Anorthosites/Syenites	granic	2071	zircon (n = 0)	12
FC-1	anorthosite	1099	zircon (n = 11), baddeleyite (n = 4)	14,15
91500/ KL	syenite	1065.4	zircon (n = 6)	16
Pacoima Canyon Pegmatite	syenite	1200	zircon $(n = 0)$	17
Other accessory phases	Sychic	1200	zircon (n = 1)	17
BLR-1	metamorphic megacryst	1047.1	titanite $(n = 2)$	18
Jumbo Black	skarn	-	garnet $(n = 2)$	-
King Island (KI-88)	skarn	_	garnet $(n = 1)$	_
Durango	volcanic iron deposit	31.44	apatite $(n = 1)$	_ 19
McClure	hbl-bt-syenite	523.5	apatite $(n = 1)$ apatite $(n = 1)$	20
MAD2	carbonatite	523.5 474.25	apatite $(n = 1)$ apatite $(n = 1)$	20 21
Kovdor	carbonatite	379.1	baddeleyite $(n = 1)$	22
		379.1 35–24	baddeleyite $(n = 1)$ baddeleyite $(n = 1)$	23
Burma/Myanmar	metamorphic belt			23 24
Phalaborwa	carbonatite	2060.6	baddeleyite $(n = 1)$	24

1) Underwood et al. (2012); 2) Hildreth (2004); 3) Hildreth and Wilson (2007); 4) Crowley et al. (2007); 5) Schmitz and Bowring (2001); 6) Chen and Moore (1982); 7) Hirt (2007); 8) Lewis et al. (2021); 9) Bucholz et al. (2014, 2017); 10) Butler et al. (2002); 11) Black et al. (2004); 12) Bucholz et al. (2018); 13) Nabelek et al. (1992); 14) Paces and Miller (1993); 15) Ibanez-Mejia et al. (2014); 16) Wiedenbeck et al. (1995, 2004); 17) Barth et al. (2001); 18) Aleinikoff et al. (2007); 19) Chew et al. (2016); 20) Schoene and Bowring (2006); 21) Thomson et al. (2012); 22) Rodionov et al. (2012); 23) Davies et al. (2018); 24) Reischmann (1995).

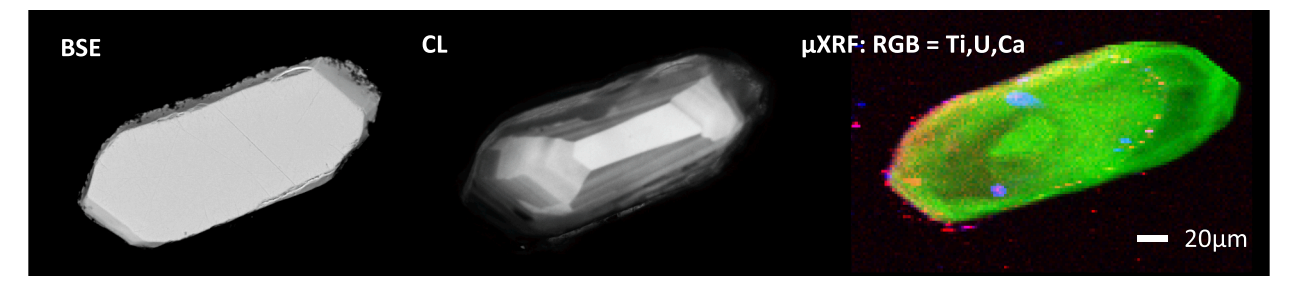


Fig. 1. Example of imaging methods used prior to XAS analysis. All images are of zircon sample Ec_zrc_2-3 from the Ecstall pluton. The μ XRF map visualizes the Ti K α , U L α , and Ca K α emission intensities.

mapping and XAS analyses at 17.5 keV probes into the interior of the crystal ($\sim\!150~\mu m$ attenuation length) while mapping at lower energy (3.76 keV) only probes the near surface of the grain ($\sim\!2~\mu m$ attenuation length). Fig. 1 shows an example of the imaging procedure conducted for each grain prior to collection of spectra for XANES/ EXAFS analyses. SEM and μXRF images of all analyzed grains are provided in the Supplementary Materials.

2.4. X-ray absorption spectroscopy (XAS)

X-ray absorption spectroscopy (XAS) is an ideal method for studying element oxidation states as the X-ray beam can be finely tuned to precise energies, and thus, used to target specific electronic transitions in individual elements. When the energy of the incident beam matches the energy required to excite a core level electron to a specific bound state, a sudden rise in X-ray absorption is seen (i.e., sharp peak) in the XAS spectrum. The energy at which this peak occurs depends on the oxidation state of the element being interrogated, with higher oxidation states shifting the absorption peak to higher energies. This prominent peak is often referred to as the "white-line" ($E_{\rm wl}$), a term which originates from the early days of X-ray spectroscopy when spectra were recorded onto photographic film and the sharp absorption peaks were expressed as heavily exposed lines on the developed film. Analysis of oxidation states utilizing the features around the peak is referred to as X-ray absorption near-edge structure (XANES) spectroscopy. For U, there is a shift in Ewl between U^{IV} and U^{VI} on the order of 2 eV for the M₄-edge and 4 eV for the L₃-edge. While the U L₃ absorption edge has a larger shift between \textbf{U}^{IV} and \textbf{U}^{VI} , the U $M_{\text{4}}\text{-edge}$ absorption peak is significantly narrower due to a smaller core-hole lifetime broadening (~7.4 eV vs 3.2 eV, respectively), since the M₄-edge probes the 5f unoccupied states of the U atom. XANES spectroscopy of the lower energy U M₄-edge thus provides better sensitivity for determining the U oxidation states in a sample (Kvashnina and Butorin, 2022). The higher energy transition of the L3-edge, however, is better suited for extended X-ray absorption fine structure analysis (EXAFS). This technique utilizes the post-edge features that arise due to scattering between the target atom and its neighbors to provide structural information on the distances, identity, and coordination of the neighboring atoms. As with mapping at low vs. high energy, analysis of the U M₄-edge will interrogate the near surface of the sample, while the higher energy of U L3-edge analyses will penetrate deeper and interrogate a larger sample volume.

The smaller excitation volume of the U M₄-edge makes this method particularly amenable to zircon studies as the measured U valence will be more closely related to textural and compositional features observed in CL images and information gained from other *in situ* analyses (*e.g.*, SIMS, LA-ICPMS). In this study, conventional total fluorescence yield U M₄-edge spectra were collected for all grains and U L₃-edge spectra were collected on a subset of the samples. From the larger sample set, FC-1, FCT, Bishop Tuff, and Ecstall zircons were selected for EXAFS analyses as these samples cover a range of host rock compositions and, except for the Ecstall zircon, have been well-characterized for ages and TREE (trace and rare-earth elements) in numerous prior studies (*e.g.*, FC-1: Orihashi et al., 2008; Ibañez-Mejia et al., 2014; FCT: Schmitz and Bowring, 2001; Gleadow et al., 2015; Bishop Tuff: Crowley et al., 2007; Trail et al., 2015).

In theory, high energy resolution fluorescence detection (HERFD) XANES can provide higher resolution at the U $\rm M_4$ -edge compared to the traditional total fluorescence yield XANES techniques used in this study (e.g., Kvashnina and Butorin, 2022). However, for samples with ppm level U concentrations such as zircon, the improved resolution would increase acquisition time from minutes to hours per spectra at the beamline used and thus significantly reduce the number of samples measurable in each beamline session. For example, a study of U speciation in contaminated wetland soils (Le Pape et al., 2020) collected 20–25 scans of 20 min each to produce spectra with low signal to noise ratios at U concentrations of ~2000 ppm, equating to >6 h per sample.

As one of the aims of the present study is to assess the extent of U valence variability in zircon and other accessory phases from different lithologies, tectonic settings, and time periods, a large number of samples need to be analyzed. Since conventional U M_4 -edge XANES is suitable for distinguishing U oxidation states, this approach was used here to allow the requisite number of samples (>150 grains) to be analyzed in the time available. Although recent improvements at several beamlines worldwide allow for faster HERFD acquisition time on low-concentration samples, the size of the beam at these end stations are generally $\geq\!100\,\mu m$ in diameter. Since most zircon grains are $\sim\!100\!-\!500\,\mu m$ in length and often contain distinct growth regions and inclusions, a beam size of 10s of μm or less is required for targeted analyses. While not yet advantageous, it is certain that as beamline capabilities continue to improve, future work utilizing HERFD XANES will further enhance our knowledge of U speciation in these minerals.

XAS analyses were performed during 4 sessions at APS Beamline 13-ID-E (GSECARS) (Sutton et al., 2017). Beamline sessions took place in March 2021, September 2021, November 2022, and March 2023. Except for the first session, all measurements were made with samples enclosed within a He atmosphere to reduce atmospheric attenuation and increase signal intensity. Incident energy was selected using a Si (111) doublecrystal monochromator calibrated to put the maximum of the first derivative of $\mu(E)$ for an Fe foil at 7110.75 eV. The beamline regularly monitors this calibration. If the Fe K edge changed by more than ± 0.5 eV between sessions, a calibration with multiple foils was redone. For reference, a Y foil was measured at the start of each session so that data could be easily compared with spectra collected at other beamlines. The maximum of the first derivative of $\mu(E)$ for the Y foil was measured at $17.044 \text{ eV} \pm 0.25 \text{ eV}$ across all sessions. XAFS data were collected in fluorescence mode using the SX7 solid state detector and all spectra were corrected for detector dead time. Measured spectra were normalized to incident intensity (I₀) measured in a He-filled, 200 mm-long ion chamber, just upstream of the KB mirror optics.

For both the U M₄- and L₃-edge, energy was scanned in 2 eV steps in the pre-edge region (U M_4 : ~3700 eV to 3718 eV; U L_3 : ~17,066 eV to 17,151 eV) and in 0.25 eV steps around the edge (U M₄: 3718 eV to 3743 eV; UL₃: 17,151 eV to 17,181 eV). In the post-edge region, energy was scanned in steps of 0.05 $\mbox{\normalfont\AA}^{-1}$ for the U $M_4\text{-edge}$ and 0.08 $\mbox{\normalfont\AA}^{-1}$ for the U $L_3\text{-}$ edge. This results in a progressively increasing step size moving away from the edge towards higher energy and allowed for high-resolution scans in the regions of greatest interest (around the peak and near post-edge), while keeping the overall time per scan to a minimum. The dwell time at each energy step was 3 s for the U M₄-edge and 2 s for the U L3-edge. The number of spots analyzed on each mineral grain varied depending on sample homogeneity. In most cases, only one or two spots were measured on each grain. The number of scans per spot also varied, with high-U grains requiring fewer scans to produce robust spectra. At the M₄-edge, we found that for zircons with typical U concentrations (100s of ppm or more) one scan per spot was typically sufficient to characterize the U oxidation state. All M₄- and L₃-edge spectra collected for an individual grain were averaged together to provide a single spectrum per crystal. Data processing (normalization, peak fitting, PCA, EXAFS transforms, FEFF fitting) was performed using the XAS Viewer program contained within the Larch software package for XAS analysis (Newville, 2013).

2.5. M₄-edge XANES data reduction

Uranium M_4 -edge spectra were normalized with a linear function in the pre-edge, but due to variations in the shape and intensity of features in the post-edge region they could not be consistently normalized by their edge jump height. Instead, these data were normalized by their maximum intensity resulting in spectra with a peak height of ~ 1 for easy comparison between samples. A limited number of spectra had anomalous features in the pre-edge region due to diffraction artifacts caused by the proximity of the XANES spot to pre-existing LA-ICPMS pits. These

spectra were discarded and are not discussed further.

To determine the E_{wl} , spectra were fit in XAS Viewer using a pseudo-Voigt function with a linear background to model the main spectral peak. The E_{wl} was taken as the centroid of the fit. Fits were also performed using Gaussian and Lorentzian functions; however, the pseudo-Voigt gave consistently better fits (lower χ^2) compared to the other peak shapes. Spectra were fit in the near-edge region from 3715 eV to 3735 eV. Examples of normalized M₄-edge spectra and their best fits are shown in Fig. 2. The quality of the spectra shown in Fig. 2 are typical for grains with high U concentrations (~5000 ppm; Fig. 2a) and moderate U concentrations (~100 ppm; Fig. 2b) (Lewis et al., 2021).

2.6. L3-edge EXAFS analysis

 L_3 -edge spectra were normalized by fitting linear functions to both the pre-edge and post-edge regions from approximately -90 to -35 eV below the edge and +250 to +550 eV above the edge. Using the Larch software package (Newville, 2013), spectra were converted to the EXAFS function, $\chi(k)$, where k is the wave number of the photoelectron emitted by the absorbing atom. Fourier transforms of the spectra were used to translate $\chi(k)$ to $\chi(R)$, where R is the distance (in Å) from the absorbing atom. Theoretical EXAFS oscillations were then calculated from crystallographic information using the FEFF8 program (Ankudinov et al., 1998; Rehr et al., 2009), which models scattering of the emitted photoelectron from the absorbing atoms based on inputs of crystallographic information and the identity of the absorbing atom. For a detailed explanation of EXAFS fitting and interpretation in Larch see Newville (2013, 2014) and Newville and Ravel (2020). Initial FEFF

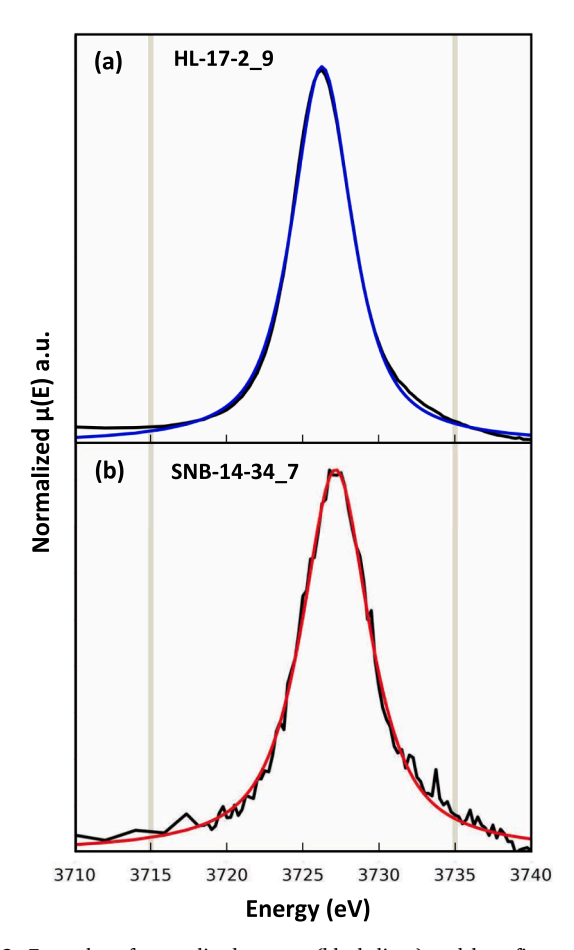


Fig. 2. Examples of normalized spectra (black lines) and best fit curves for zircon grains with **(a)** high U concentrations (blue line: HL-17-2_9 \sim 5000 ppm U) and **(b)** low U concentrations (red line: SNB-14-34_7 \sim 100 ppm U). Vertical lines show the bounds of the fit.

calculations were run using zircon structural information contained within the Larch library from Hazen and Finger (1979) that were modified to reflect U substitution at the Zr site. Fourier transformed spectra were fit from 1 Å to 4 Å in $\chi(R)$ space (Fig. 3c) using three single scattering paths (U-O, U-Si, and U-Zr). Due to the limited k-range of the data used for fitting (<10 Å $^{-1}$) the maximum resolution between atomic neighbors is \sim 0.2 Å, which is greater than the separation of the two reference Zr-O distances of 2.11 Å and 2.26 Å (Hazen and Finger, 1979). For this reason, only one U-O scattering path was used in the fit to determine the average U-O bond length in each sample. Examples of the normalization procedure, extracted EXAFS oscillations, and FEFF fitting results are shown in Fig. 3. All U L₃-edge spectra used for EXAFS analysis are available in the Supplementary Materials.

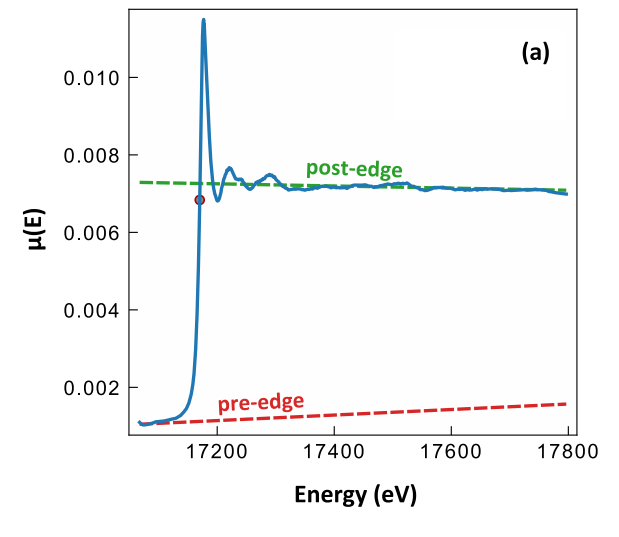
2.7. Anisotropy tests on U M4-edge spectra

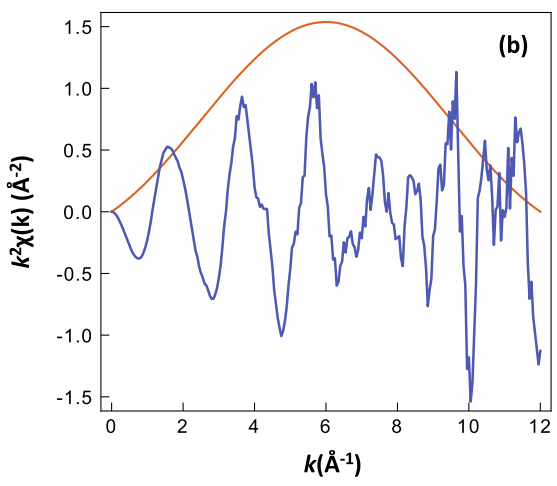
In anisotropic minerals such as zircon, measured X-ray absorption spectra can be affected by differences in crystallographic orientation of the crystal being analyzed relative to the polarization direction of the incident X-ray beam leading to dichroism (Brouder, 1990). To test the possible effect of this phenomenon on measured U M₄-edge zircon spectra, two grains from three samples (Bishop Tuff, Fish Canvon Tuff, and Ecstall pluton) were mounted such that their c-axis was either parallel or perpendicular to the sample surface. These grains were then repeatedly analyzed at the same spot location through a series of stage axial rotations (0, 45, and 90 degrees). In addition, three randomly oriented FC-1 zircon grains were analyzed at the same spot location at stage rotation angles of 0° and 90°. While many zircon grains have a well-developed crystal habit and are typically mounted with the c-axis parallel to the sample surface, FC-1 zircon grains are almost always anhedral and thus mounted in random orientations relative to the sample surface. Comparison of the large number of spectra collected on FC-1 zircon grains thus allowed investigation of a variety of geometries between the incident beam and the zircon crystallographic axes.

2.8. Raman spectroscopy

Raman spectroscopy has proven a useful method for assessing the extent of radiation damage (due to radioactive decay) in a zircon crystal as the peak width and center of the Raman bands widen and shift to lower wavenumbers, respectively, with increasing metamictization (e.g., Nasdala et al., 1995; Palenik et al., 2003; Marsellos and Garver, 2010; Anderson et al., 2020). High U concentration can also distort the crystal structure of zircon and lead to widening of Raman peaks, but this effect is much smaller than the peak broadening due to radiation damage (1s of wavenumbers opposed to 10s). More importantly, previous studies of U oxidation states in zircon have indicated that metamictization may lead to an increase in the proportion of U^{IV} at the expense of higher valence U within amorphous zones (Zhang et al, 2003), which could complicate the interpretation of our XANES results (see Section 4.1 for discussion). The same test cannot be performed on other accessory phases due to the lack of a calibration between Raman spectral modifications with alpha fluence, so we cannot ascertain whether the redox states of U in the other accessory phases are primary features or due to some post-crystallization secondary process.

Raman spectra were collected using a Renishaw inVia Raman spectrometer at Caltech (Rossman laboratory) over the range 200–1100 cm $^{-1}$ using a 514 nm laser and a 3000 lines/mm grating. Calibration of the instrument was performed by measuring a Si-wafer and setting the centroid of the prominent Raman band to 520.5 cm $^{-1}$. Measurements were made in air and at ambient temperature using an exposure time of either 1 or 2 s and with 20–60 scans collected at each spot depending on the crystallinity of sample (more crystalline samples required fewer scans to produce robust spectra). Raman spots were placed near the location of the XAS measurements when possible. Overall, 1–5 spectra were obtained for each grain depending on the intensity of the Raman





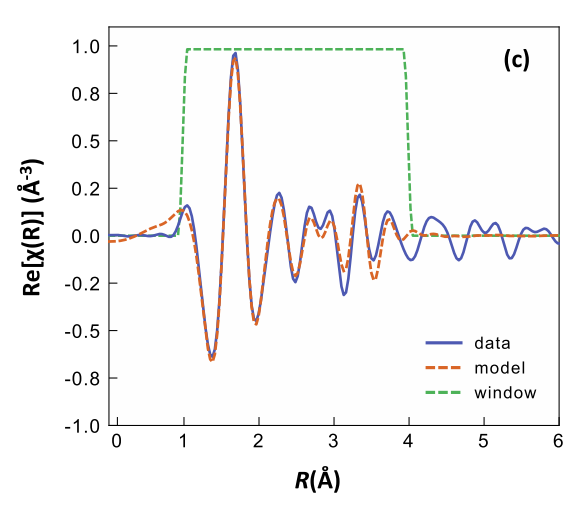


Fig. 3. Example of U L_3 -edge normalization and EXAFS data processing for zircon FCT 2-1. (a) Raw $\mu(E)$ with the pre- and post-edge functions used for normalization. (b) Extracted EXAFS oscillations and window used for the Fourier transform. (c) Data and best fit from FEFF modeling.

signal above background. For samples where multiple spectra were collected, the values for the peak widths and Raman shifts were averaged together.

The intensity of the various peaks in a Raman spectrum can be highly dependent on the orientation of the crystal and may be absent altogether in some beam-sample geometries (Dawson et al., 1971; Anderson et al.,

2020). We focused on the \sim 356 cm⁻¹ E_g vibrational band as this was the most common feature observed in our samples. While the 1008 cm⁻¹ Raman band has traditionally been used to assess radiation damage, Anderson et al. (2020) showed that the 356 cm⁻¹ E_g band spans a greater range in full-width at half maximum (FWHM) values indicating that it may be a more useful indicator of radiation damage. Raman peaks were fit using a Gaussian approximation to determine the FWHM and center of each feature. The average 2 standard deviation (SD) uncertainty was determined from multiple measurements on the same grain of the E_g band. For radiation damaged zircon, the uncertainty on the peak width and center of the E_g band are 6 cm⁻¹ and 2 cm⁻¹, respectively. Crystalline zircon gave more consistent results with an uncertainty of 0.4 cm⁻¹ for both parameters.

3. Results

3.1. U M₄ XANES data consistency & uncertainties

Since data were acquired during multiple session over the span of two years, tests were performed to assess data stability and reproducibility over time. FC-1 zircon was selected as a reference material for this purpose as these crystals appear homogenous in CL images and showed the most consistent spectra amongst samples measured during the first analysis session. As shown in Fig. 4a, the measured U M_4 -edge E_{wl} of FC-1 zircon is reproducible within ± 0.18 eV (2SD). This value is larger than the typical 2 SE error of ± 0.03 eV reported by XAS Viewer for the centroid of the fit used to determine the E_{wl} , but we argue that it better represents the precision of an individual measurement on a natural zircon. Indeed, the MSWD of all FC-1 measurements calculated using a 2 SD for each data point of ± 0.03 eV or ± 0.18 eV are, respectively, 37.53 and 1.04, meaning that a large amount of the variance is unexplained if the smaller uncertainty is used. We thus applied a ± 0.18 eV uncertainty to all measurements of individual zircon grains. Where the average E_{wl}

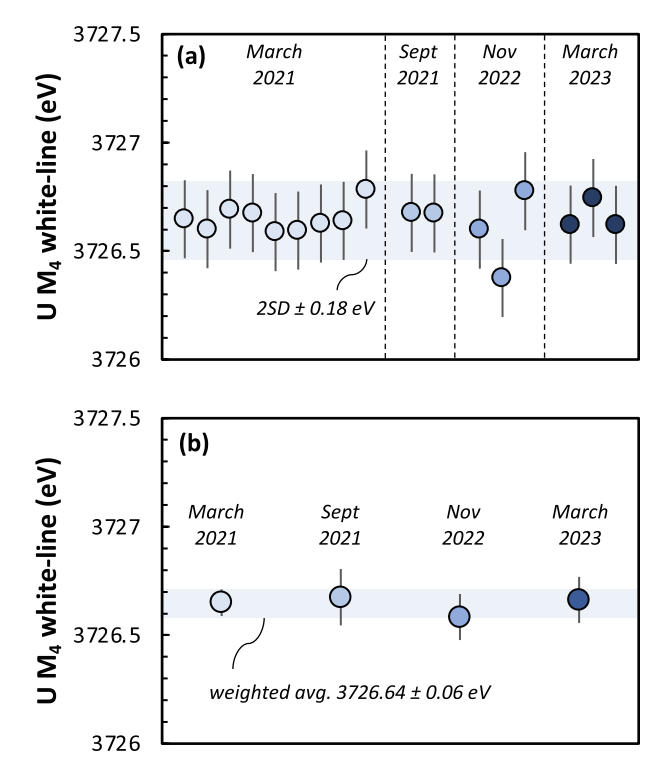


Fig. 4. (a) White-line energy of individual FC-1 zircon grains measured during each analysis session. Colored bar represents the ± 2 SD uncertainty of the data across all sessions (± 0.18 eV). (b) Average white-line energies of FC-1 zircon measured during each analysis session. Vertical error bars are the 2 SE uncertainty for that analysis session.

for a sample, calculated from measurements of multiple grains, is discussed, the 2 SE uncertainty is used instead: i.e., $2\,\mathrm{SD}/\sqrt{n}$, where n is the number of grains analyzed. Comparison of the average U $\mathrm{M_4}$ -edge $\mathrm{E_{wl}}$ of FC-1 zircon obtained in each session shows stability within <0.1 eV (Fig. 4b). Given the stability and reproducibility of FC-1 zircon white-line energies, along with their broad availability as a common laboratory reference material for U-Pb geochronology and Lu-Hf isotopes, we recommend that grains of FC-1 zircon also be used as a reference material for future U XANES studies of zircon. Raw FC-1 material can be obtained by contacting the Arizona LaserChron Center at University of Arizona.

The effect of beam damage on U oxidation states in zircon was assessed by comparing successive XANES scans collected at the same location. Fig. 5 shows the results of this test for two zircon grains over the course of three scans. No change in the measured U valence was detected across the repeated scans with the fitted E_{wl} value varying by only ± 0.04 eV (2 SD), indicating that U oxidation states in zircon are not affected by beam-induced damage at the U M₄-edge energy.

3.2. U M₄-edge XANES E_{wl} and calculated U valence

Average U M₄-edge spectra for all mineral grains analyzed in this study are shown in Fig. 6 (zircon) and Fig. 7 (titanite, baddeleyite,

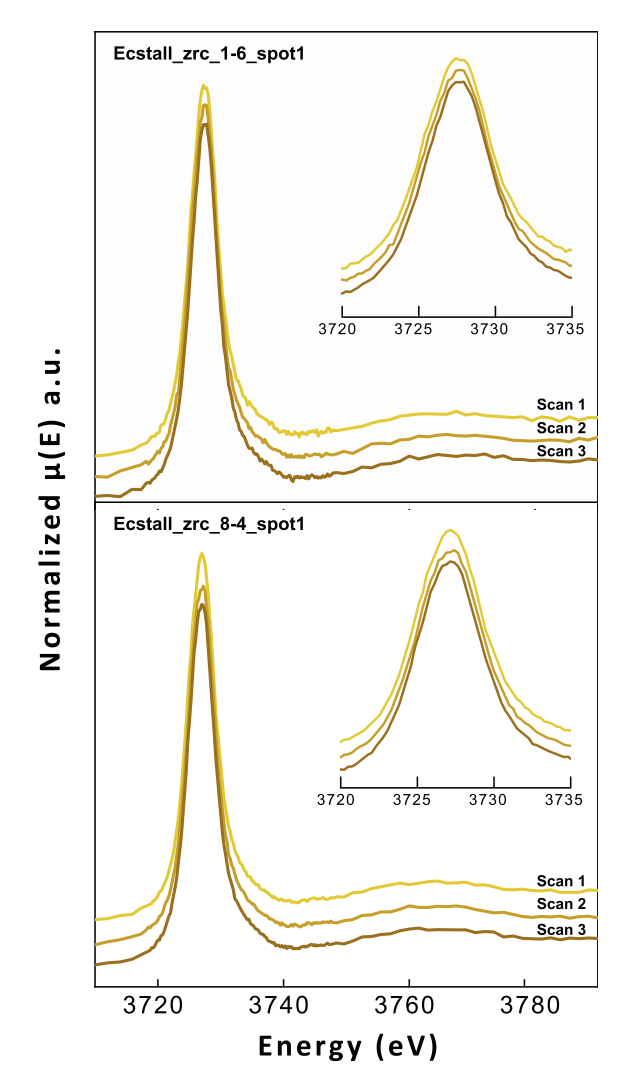


Fig. 5. Results of repeated XANES scans at the same location for two zircon grains. The variation in fitted E_{wl} varies by ± 0.04 eV (2 SD) between the three scans indicating that beam damage does not affect U oxidation states in zircon.

apatite, garnet). Due to the large number of samples analyzed in this study, however, we focus on the white-line energy of each spectrum as a proxy for the proportion of the different U oxidations states present in a sample. This allows each spectrum to be represented by a single value that can be plotted against other parameters and provides a simplified means of representing the data. Details regarding the calculation of average U valence from U M_4 $E_{\rm wl}$ are given below.

Fig. 8 shows the white-line energies (E_{wl}) of all U M₄-edge spectra collected for each grain analyzed in this study. Data points represent the average Ewl of all spectra collected for an individual grain. The dashed lines in Fig. 8 show the approximate positions of the U^{IV}, U^V, and U^{VI} edges. The position of the U^{IV} edge was determined from the E_{wl} of UO₂ (3726.2 eV) and the energy of the UV and UVI edges are placed at 1.5 eV and 2.0 eV above this value, respectively, based on data presented by Kvashnina and Butorin (2022) (Table 2). While the HERFD spectra they present display narrower peaks and improved resolution of post-edge features compared to the traditional U M4-edge XANES spectra in this study, the difference in Ewl between our most reduced and oxidized samples is similar to that reported between pure U^{IV} and U^{VI} compounds (\sim 2.0 eV). Additionally, several other studies have found the UV edge to be ~75 % between the U^{IV} and U^{VI} edges (Table 2) (Kvashnina and Butorin, 2022, Leinders et al., 2017; Popa et al., 2016; Halse, 2014), suggesting that the E_{wl} position we assume for U^V is also a reasonable

Of all mineral phases investigated, zircon shows the greatest variability in $E_{\rm wl}$ (~2.0 eV) with samples having spectra consistent with U valence spanning the range from fully reduced (U^{IV}) to fully oxidized (U^{VI}) . Apatite and baddeleyite display a narrower range of E_{wl} (~0.6 eV and \sim 0.5 eV, respectively), with average values \sim 0.5 eV above the U^{IV} Ewl value, indicating that these phases also incorporate a component of more oxidized U. Titanite samples have the lowest Ewl of the samples measured (3726.3 eV average) and show a restricted range in peak energy of ~0.2 eV, indicating that titanite incorporates only U^{IV}. Importantly, this restricted range of white-line energies is observed in titanite grains from both the Fish Canyon Tuff and Ecstall localities, while zircon from these same samples indicate a large proportion of oxidized U being present: i.e., even in the presence of oxidized U, titanite only incorporates UIV in its crystal lattice. The two garnet samples measured yield E_{wl} consistent with a dominantly U^{IV} valence, however, these two grains are both andradite garnets separated from skarns. Since garnet forms an array of different solid solutions and can form in a variety of environments, these two samples are not necessarily reflective of U oxidation states in all types of garnet.

As further indication that zircon can contain multivalent U, we examine the variation in the full width at half-maximum (FWHM) of zircon U M4-edge spectra. Fig. 9 plots the FWHM of individual spectra against their white-line energies and shows that the lowest FWHM values occur near the nominal edge energies of the U^{IV} and U^{VI} ions and the highest values occur in between these energies. The FWHM at the low energy end of the range (U^{IV}) is ~4.6 eV and increases to a maximum of ~5.6 eV between the U^{IV} and U^{V} peaks before decreasing to a minimum of \sim 4.7 eV at the energy of the $U^{\hat{V}}$ peak. Peak widths at this energy, however, vary from approximately 4.7 eV to 5.2 eV. Between the U^{V} and U^{VI} edges the width varies from 5.2 eV to 4.5 eV and reaches a minimum of \sim 4.4 eV at the energy of the U^{VI} edge. The observation that the narrowest peak widths occur near the white line energies obtained for zircon samples with pure U^{IV} or U^{VI} content, and the broadest peaks occur between these values, suggests that the latter are composed of multiple, convoluted, spectral peaks. Since a spectrum with a mixed U^{IV} + U^{VI} composition will lead to a broader peak compared to a mix of U^{IV} + U^V, the variability in the FWHM at intermediate white-line energies in Fig. 9 may suggest that samples with a broader peak (e.g., HLMC, light blue circles) are predominantly a mixed U^{IV} and U^{VI} composition, while conversely, samples with a lower FWHM are likely a mix of U^{IV} and U^V (e.g., Harney Peak, green circles).

For illustrative purposes, the averaged U M₄-edge spectra for all

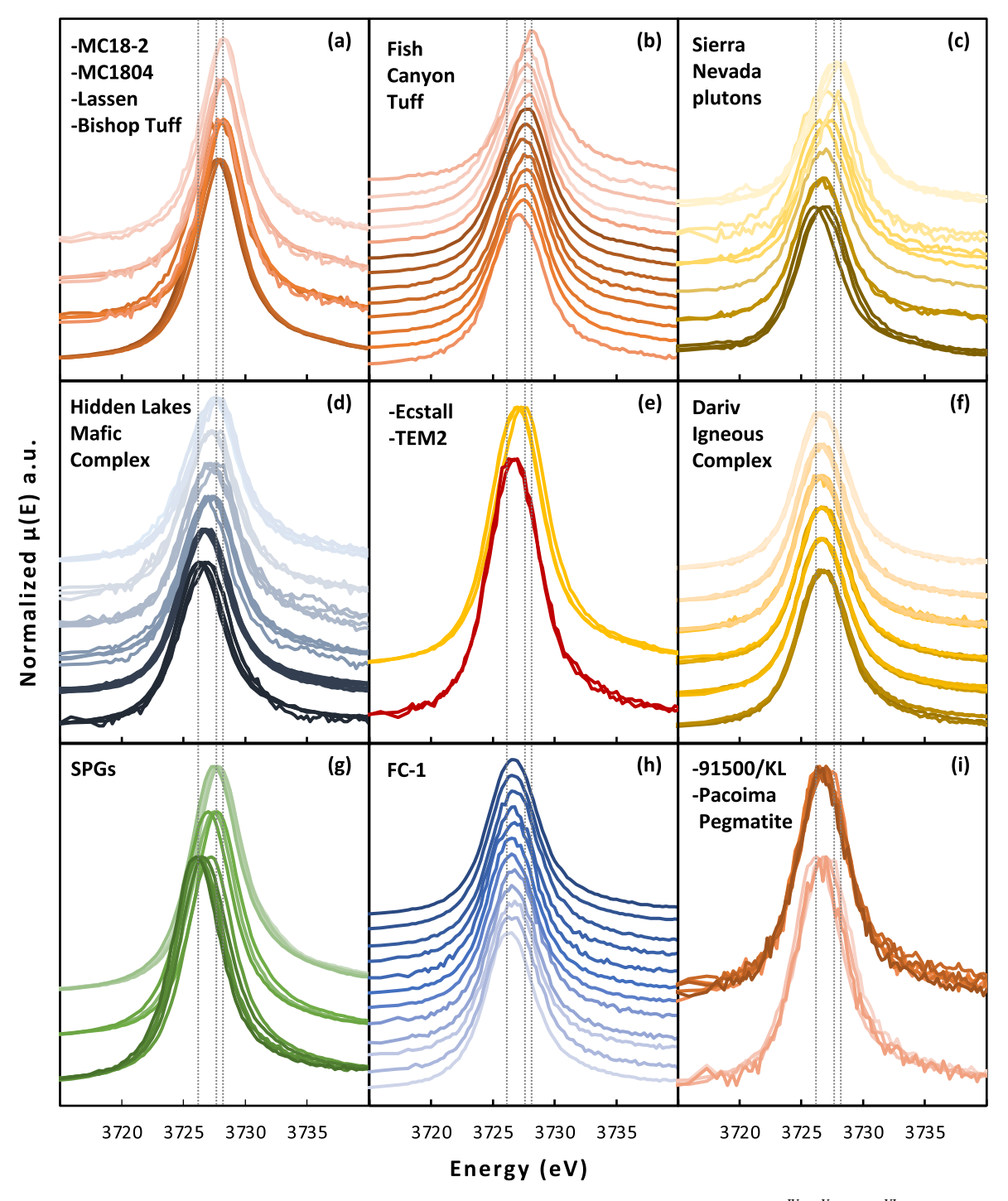


Fig. 6. Normalized U M₄-edge spectra for all zircon grains. Dotted lines show the approximate edge energies of the U^{IV}, U^V, and U^{VI} ions (from left to right, respectively). From top to bottom: (a) MC18-04, MC18-02, LF042-02, Bishop Tuff; (b) Fish Canyon Tuff; (c) Bullfrog, Dragon, Independence, Mt. Whitney, Lone Pine, Paradise; (d) SNB-16-12, SNB-16-9, SNB-14-34, SNB-16-6, SNB-14-40, HL-17-2; (e) Ecstall, TEM2; (f) MO-11-14, MO-11-12, MO-11-16, MO-11-19, MO-11-23, MO-11-26; (g) HP44A, HP21C, SP-16-52; (h) FC-1; (i) 91500/KL, Pacoima Pegmatite.

titanite samples as well as for zircon grains from samples HP44A (Harney Peak) and MC18 (Long Valley) are shown in Fig. 10. These spectra were chosen as they are representative of endmember samples from our dataset with predominantly U^{IV} , U^V , and U^{VI} valences, respectively. Average titanite and MC18 spectra were chosen to represent U^{IV} and U^{VI} as theses samples have the lowest and highest E_{wl} amongst our samples, respectively. Additionally, the MC18 spectrum shows a slight asymmetry on the high-energy side of the peak that is likely due to U^{VI} (Fig. 10 inset). HERFD spectra of U^{VI} compounds often exhibit additional

shoulders and peaks in the post-edge region, and while these features are obscured in the traditional XANES spectra collected in this study, the slight shoulder in the MC18 spectra suggests the presence of U^{VI} in these samples. HP44A was selected to represent U^{V} as its E_{wl} occurs near the nominal energy of the U^{V} edge (\sim 75 % between U^{IV} and U^{VI} at 3727.7 eV), and of the samples with E_{wl} around this value, HP44A zircon have the narrowest FWHM. Additionally, U^{V} has been previously observed in zircon (Vance and Mackey, 1974; Zhang et al., 2003).

To confirm that all three valence states of U are indeed present in our

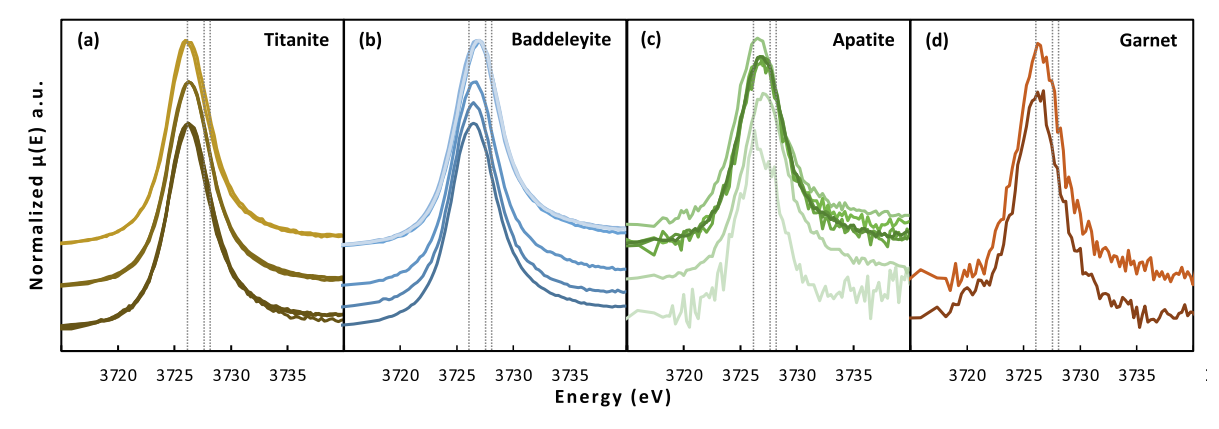


Fig. 7. Normalized U M₄-edge spectra for all titanite, baddeleyite, apatite, and garnet grains. Dotted lines as in Fig. 5. From top to bottom: (a) BLR-1, Ecstall, Fish Canyon Tuff; (b) FC-1, Kovdor, Phalaborwa, Burma; (c) Durango, Fish Canyon Tuff, MAD2, McClure; (d) Jumbo Black, KI-88.

data set, we performed a principal component analysis (PCA) on a set of U $\rm M_4$ spectra comprising those shown in Fig. 10, along with the average spectra for zircon from felsic volcanic rocks, arc-related rocks, SPGs, and anorthosites + syenites were analyzed (Fig. 11a). PCA was performed on this set of endmember and average spectra to reduce the number of non-significant components arising from noise in the spectra of individual grains while maintaining the variability observed in the dataset. Since PCA can be sensitive to normalization, several trials were run varying slightly the pre- and post-edge normalization ranges of the U $\rm M_4$ spectra. In all trials PCA identified at least three significant components (average variances of 72 %, 25 % and 3 %) whose total variance accounts for >99 % of the variance in the data set (Table S1, Fig. 11b), confirming that all three valence states of U are present within the sample set as a whole.

To constrain the average U valence (Uⁿ⁺) of our zircon samples, their U M₄ spectra were fit using a linear combination of the spectra shown in Fig. 10, which were chosen to represent the U^{IV}, U^V, and U^{VI} endmembers (titanite, HP44A zircon, and MC18 zircon, respectively). The results from these analyses (Fig. S2) are consistent with the FWHM values presented in Fig. 9, as the spectra at intermediate white-line energies with the greatest widths are best fit by a combination of U^{IV}, U^V, and U^{VI}, while spectra with narrower peaks but similar Ewl are best fit by a combination of predominantly U^{IV} and U^V. While the proportions of each U oxidation state we determined can vary at a given Ewl (i.e., can be a mix of U^{IV}, U^V, and U^{VI} or only two of these oxidation states), the average Uⁿ⁺ calculated for each sample varies predictably with the E_{wl} of their spectra (Fig. 12). Since the difference in energy between the U^{IV} and UV edges is larger than the difference between UV and UVI (1.5 eV vs 0.5 eV, respectively) the variation in Uⁿ⁺ with E_{wl} is not expected to be linear, and as such, the following function was used to model the data:

$$U^{n+} = a e^{\left[\frac{E_{wl} - E_{U(IV)}}{b}\right]} + c \tag{1}$$

where a, b, and c are the fitted parameters, E_{wl} is the white-line energy and $E_{U(IV)}$ is the E_{wl} of a reference U^{IV} compound. A best fit to the data is shown by the black curve in Fig. 12 and given below (Equation (2)):

$$U^{n+} = 0.53 e^{\left[\frac{E_{wl} - 3726.2}{1.38}\right]} + 3.54 \pm 0.13 (2\sigma) \tag{2} \label{eq:2}$$

Since measured E_{wl} values can vary slightly between beamlines depending on the calibration used, the U^{n+} values for each sample, calculated using Eq. (2), are discussed for the remainder of the text except where specific E_{wl} values are relevant. Average E_{wl} values and calculated U^{n+} values for zircon samples are given in Table 3.

Amongst the zircon grains analyzed, those from arc-related magmas show the most variation in U^{n+} , with zircon grains spanning the entire valence range from U^{IV} to a mixed U^V and U^{VI} oxidation state. Zircon

from the southern Sierra Nevada plutons vary considerably between samples and suggest that crystallization in these plutons occurred under different redox conditions. For example, zircon from the Bullfrog Pluton have the highest U oxidation states measured for a plutonic rock in this study, with an average valence of U^{5.3+}. At the low end, zircon from the Paradise and Lone Pine granodiorites and Mt. Whitney granite have average E_{wl} values that are more than 1.0 eV lower than those measured from the Bullfrog Pluton, corresponding to average U valences of U^{4.1+}, ${\bf U}^{4.3+}$, and ${\bf U}^{4.4+}$, respectively. In particular, one zircon from the Paradise granodiorite has a spectrum indicative of an entirely UIV composition. Zircon from the Hidden Lakes Mafic Complex in the central Sierra Nevada are also quite variable in their U valence, with different samples of this suite ranging from an average of U^{4.3+} to U^{5.0+}. Notably, Hidden Lakes zircon grains separated from rocks with cumulate textures have markedly lower U valence and higher U concentrations when compared to zircon from rocks with liquid-like textures (dark blue circles vs. light blue circles in Fig. 8) (Lewis et al, 2021). This result is consistent with the greater compatibility of U^{IV} over U^V or U^{VI} in the zircon structure (Burnham and Berry, 2012, Mallmann et al., 2021).

Zircon from strongly peraluminous granites (SPG) display differences in U oxidation states between grains from Archean (SP-16-52: Sturgeon Lake) and Proterozoic samples (HP44A/HP21C: Harney Peak), with the Archean grains containing a greater proportion of U^{IV} relative to the Proterozoic samples (averages of $U^{4.25+}$ vs. $U^{5.0+}$, respectively). Oxybarometry on these samples by Bucholz et al. (2018) using biotite-whole rock Fe-Mg modeling determined that the oxygen fugacity of the Archean Sturgeon Lake granite was lower than the fO_2 of the Proterozoic Harney Peak granite (FMQ+0.7 vs. FMQ+1.4, respectively). The results from this study are thus consistent with the idea that Archean SPGs are generally more reduced than their Proterozoic counterparts.

Zircons from felsic volcanic rocks have the highest U valence amongst our samples, with the peaks in their spectra predominantly between the \mathbf{U}^V and \mathbf{U}^{VI} edges, though some samples fall between the energies expected for \mathbf{U}^{IV} and \mathbf{U}^V . Zircon from the Lassen volcano and the post-caldera Long Valley eruptions have the highest U valence, close to the pure \mathbf{U}^{VI} endmember. In the presence of oxidizing fluids U is readily oxidized to \mathbf{U}^{VI} and the shallow magma chambers that feed these systems are more likely to have interacted with such fluids prior to, or during, eruption relative to deeper-seated plutonic rocks.

Finally, and contrary to samples from felsic volcanic rocks, zircons from anorthosites and syenites have average U oxidation states restricted to the lower end of the range, though their spectra are still indicative of a mixed U^{IV}-U^V composition. High K melt concentrations have been shown to have a reducing effect on U (Dominé and Velde, 1985) and may explain the more restricted range in U oxidation states observed in syenite samples relative to zircons from most of the arcrelated samples. This is supported by zircon grains from the

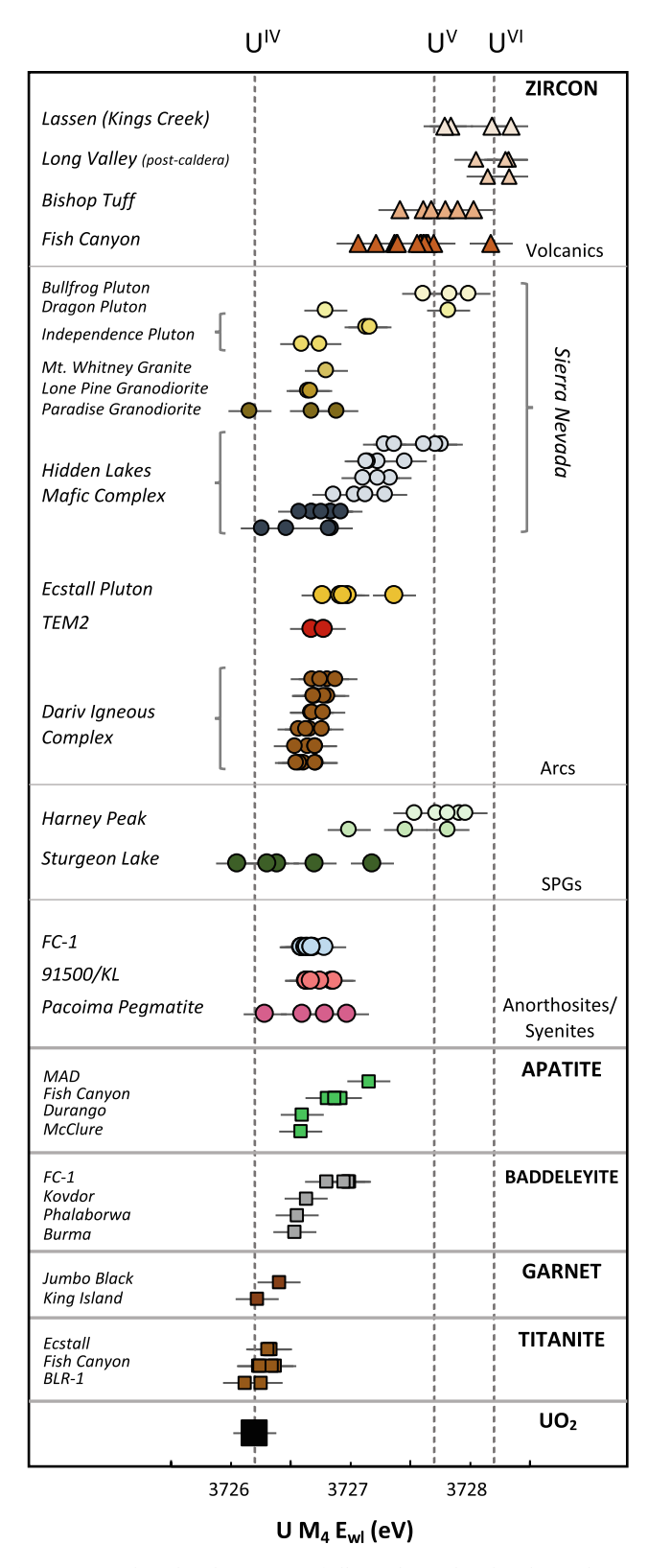


Fig. 8. U M₄-edge white-line energy of all samples analyzed in this study. Data points represent the average white-line energy of all spectra collected for an individual grain. Horizontal error bars are the 2 SD uncertainty of the peak position (± 0.18 eV). Vertical dashed lines show the approximate edge energies of the U^{IV}, U^V, and U^{IV} ions.

 $\begin{tabular}{ll} \textbf{Table 2} \\ \textbf{Published U M}_4 \, E_{wl} \, \text{values for the three U oxidation states compared with values from this study. Values are in eV.} \\ \end{tabular}$

U ^{IV}	U ^V	U ^{VI}	$(U^{V}-U^{IV})/$ $(U^{VI}-U^{IV})$	Ref.
3725.0	3726.5	3727.0	0.75	Kvashnina and Butorin (2022)
3725.2	3726.4	3726.8	0.75	Leinders et al. (2017)
3724.5	3725.5	3726.2	0.6	Popa et al. (2016)
3725.1	3726.2	3726.7	0.7	Halse (2014)
3726.20	3727.70	3728.20	0.75	This study

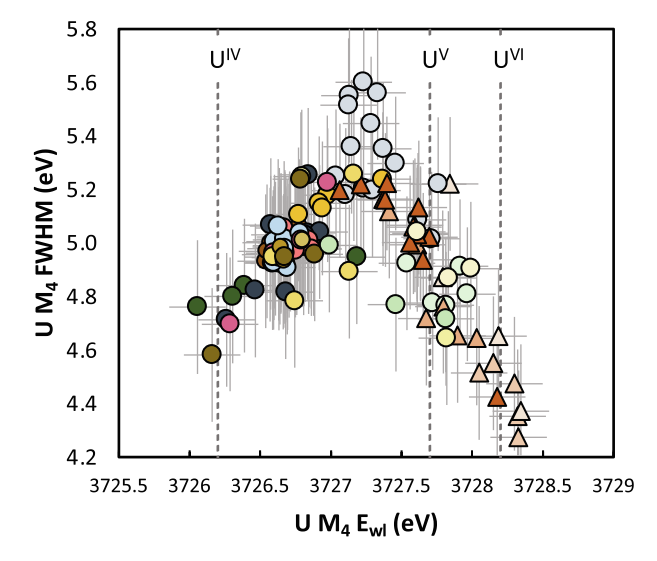


Fig. 9. Variation in U M_4 -edge FWHM with white-line energy for zircon samples. Symbols as in Fig. 8.

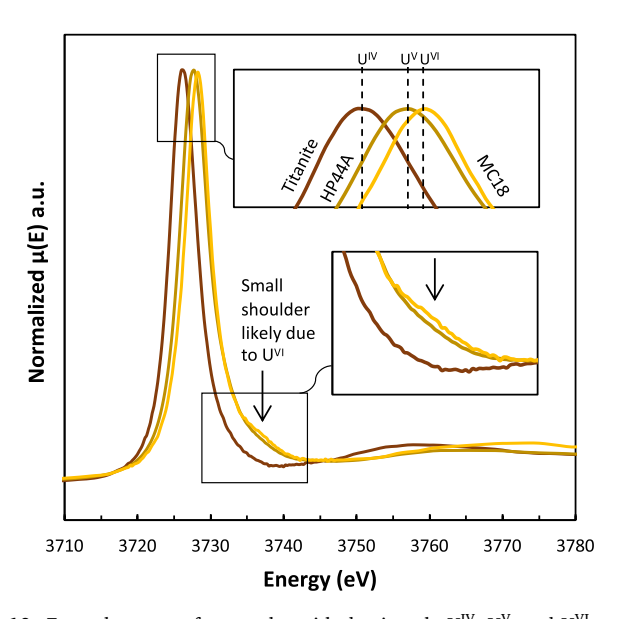
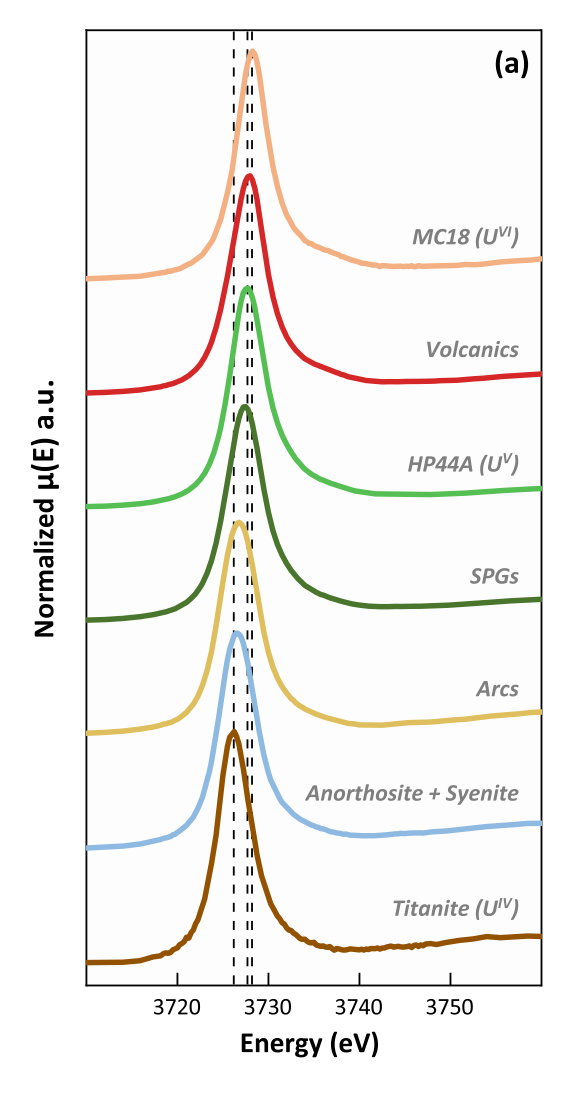


Fig. 10. Example spectra for samples with dominantly U^{IV} , U^V , and U^{VI} compositions: titanite (all samples), HP44A (zircon), MC18 (zircon), respectively. Spectra are averages of all scans collected for that sample and represent multiple grains. Note the small shoulder in the MC18 spectrum indicative of U^{VI} .

related high-K Dariv Igneous Complex (DIC) that show U valences as reduced as zircon from syenites.

3.3. U L3-edge EXAFS analysis

Although U M4 XANES is better suited for determining oxidation



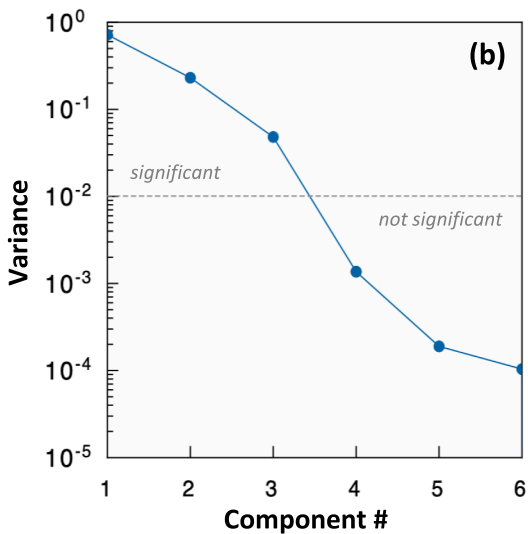


Fig. 11. (a) Average U M4-edge spectra used for principal component analysis. PCA was performed from 3710 to 3790 eV, a smaller energy range is plotted to highlight differences in $E_{\rm wl}$. (b) Example SCREE plot showing the variance of the components.

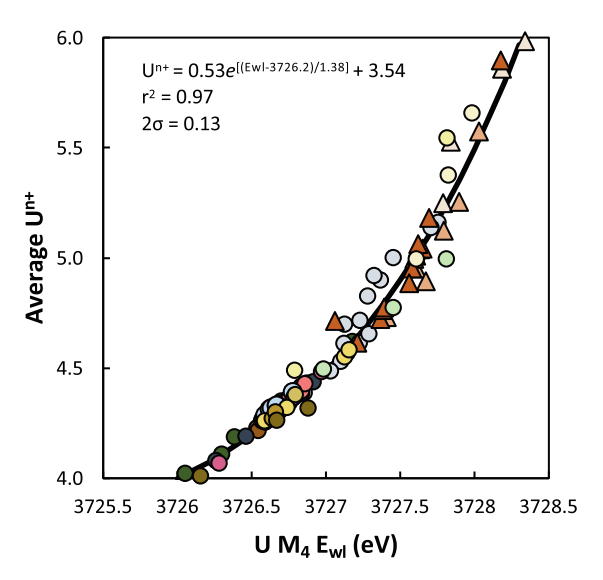


Fig. 12. Variation in average U^{n+} with E_{wl} for individual zircon samples. Black line is the best fit to the data given by Eq. (2). Symbols as in Fig. 8.

 $\label{eq:table 3} \textbf{Average} \ E_{wl} \ \text{and} \ U^{n+} \ \text{for all zircon samples}.$

Sample	Average	Average	
	E _{wl} (eV)	U^{n+}	
Volcanics			
LF042-02	3728.04	5.59	
MC18-2	3728.22	5.85	
MC18-4	3728.24	5.88	
BT	3727.74	5.18	
FCT	3727.55	4.98	
Arcs			
Bullfrog	3727.81	5.26	
Dragon	3727.31	4.81	
Independence (11SN31)	3726.67	4.30	
Independence (11SN15)	3727.15	4.60	
Mt. Whitney	3726.80	4.37	
Lone Pine	3726.66	4.29	
Paradise	3726.57	4.26	
SNB-16-12	3727.55	4.97	
SNB-16-9	3727.22	4.66	
SNB-14-34	3727.24	4.68	
SNB-16-6	3727.08	4.56	
SNB-14-40	3726.76	4.35	
HL-17-2	3726.60	4.27	
Ecstall	3726.99	4.50	
TEM2	3726.73	4.33	
MO-11-14	3726.78	4.36	
MO-11-16	3726.74	4.33	
MO-11-26	3726.66	4.29	
MO-11-23	3726.65	4.28	
MO-11-19	3726.63	4.27	
SPGs			
HP44A	3727.79	5.24	
HP21C	3727.42	4.87	
SP-16-52	3726.53	4.25	
Anorthosites/Syenites			
FC-1	3726.65	4.29	
91500/KL	3726.73	4.33	
Pacoima Pegmatite	3726.66	4.30	

states, EXAFS analysis of U L₃-edge spectra can provide important structural information, in particular, on whether the incorporation of oxidized U into the zircon lattice is accompanied by any significant structural transformations that could affect the XANES results (i.e., U^{VI} present as uranyl (UO $_2^{2^+}$) which has U-O bonds at 1.8 Å compared to $\sim\!2.2$ Å for the Zr-O bond in zircon). EXAFS analyses were performed on a subset of zircon grains from four different samples (FC-1 n = 6; FCT n

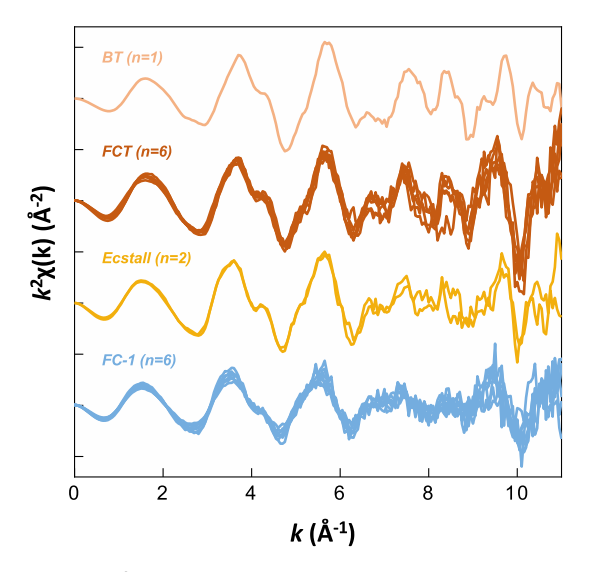


Fig. 13. k^2 -weighted EXAFS $\chi(k)$ for individual zircon grains.

= 6, Ecstall n = 2, Bishop Tuff n = 1) ranging from moderately to highly oxidized (FMQ to FMQ+2.5). The extracted EXAFS oscillations for all samples are shown in Fig. 13 (normalized U L3-edge spectra are shown in Fig. S3). The reference Zr-X interatomic distances and the U-X distances determined by FEFF fitting are given in Table 4 and shown in Fig. 14. The U-X bond distances we determine for these samples are generally larger than the reference distances (Hazen and Finger, 1979), though they tend to decrease with increasing U oxidation state, consistent with higher valence ions having a smaller ionic radii and greater attractive force relative to more reduced species. For instance, between zircon from FC-1 (mostly U^{IV}) and FCT (mixed $U^{IV} + U^{V/VI}$) the average U-O distance decreases by ~0.07 Å from slightly larger than the reference distance for FC-1 to approximately the same as the reference Zr-O distance for FCT. This result can largely be explained by the difference in radius between ${\rm Zr^{IV}}$ (0.98 Å) relative to ${\rm U^{IV}}$ (1.14 Å) and ${\rm U^{VI}}$ (1.00 Å) when in 8-fold coordination (Shannon, 1976). Overall, EXAFS analysis indicates that no significant structural transformation occurs in these samples with increasing U valence, rather, we observe a modest reduction in interatomic distances (up to \sim 3 %) with increasing valence (Fig. 14).

Table 4Reference Zr-X bond lengths and best fit values for U-X bond lengths from EXAFS analysis of U substitution in zircon. All distances are in Å.

analysis of a substitution in Enterin in abstinces are in in					
Sample	U-O	U-Si	U-Zr	s02	e0
FCT 1.2-1	2.21 ± 0.02	3.05 ± 0.03	3.71 ± 0.02	$\textbf{0.80} \pm \textbf{0.16}$	8.3 ± 1.7
FCT 1.1-7	2.18 ± 0.03	3.03 ± 0.03	3.69 ± 0.03	$\textbf{0.93} \pm \textbf{0.27}$	5.7 ± 2.6
FCT 1.6-4	2.23 ± 0.02	3.06 ± 0.03	3.72 ± 0.02	$\textbf{0.87} \pm \textbf{0.23}$	10.5 ± 2.0
FCT 1.6-7	2.22 ± 0.04	3.06 ± 0.03	3.70 ± 0.02	$\textbf{0.92} \pm \textbf{0.24}$	8.0 ± 2.2
FCT 1.8-1	2.20 ± 0.02	3.08 ± 0.05	3.65 ± 0.03	$\textbf{0.64} \pm \textbf{0.16}$	6.8 ± 2.5
FCT 2.1-1	2.20 ± 0.02	3.02 ± 0.04	3.69 ± 0.03	$\textbf{0.82} \pm \textbf{0.22}$	6.9 ± 2.6
FC1 1.3-1	2.25 ± 0.02	3.08 ± 0.03	3.73 ± 0.03	0.65 ± 0.16	$\textbf{7.4} \pm \textbf{2.0}$
FC1 1.4-5	2.26 ± 0.02	3.10 ± 0.04	3.73 ± 0.03	$\textbf{0.74} \pm \textbf{0.17}$	8.5 ± 1.8
FC1 1.9-1	2.28 ± 0.02	3.12 ± 0.04	3.71 ± 0.04	$\textbf{0.69} \pm \textbf{0.20}$	9.3 ± 2.1
FC1 1.10-7	2.26 ± 0.02	3.11 ± 0.03	3.71 ± 0.04	0.56 ± 0.17	7.9 ± 2.3
FC1 2.1-1	2.25 ± 0.02	3.09 ± 0.04	3.72 ± 0.04	$\textbf{0.80} \pm \textbf{0.22}$	7.8 ± 2.1
FC1 2.2-1	2.28 ± 0.02	3.10 ± 0.03	3.72 ± 0.03	$\textbf{0.82} \pm \textbf{0.22}$	10.9 ± 1.8
Ec 1-6	2.23 ± 0.02	$\textbf{3.04} \pm \textbf{0.03}$	3.70 ± 0.03	0.90 ± 0.27	7.5 ± 2.4
Ec 2-3	$\textbf{2.22} \pm \textbf{0.02}$	3.07 ± 0.04	3.68 ± 0.05	$\boldsymbol{0.98 \pm 0.37}$	6.4 ± 2.0
BT 1-3	2.16 ± 0.02	3.01 ± 0.05	3.66 ± 0.03	$\textbf{0.77} \pm \textbf{0.22}$	3.8 ± 2.6
Average	U-O	U-Si	U-Zr		
FCT	2.21	3.05	3.69	_	_
FC-1	2.26	3.10	3.72	_	_
Ec	2.23	3.05	3.69	_	_
BT	2.16	3.01	3.66	_	_
	Zr-O	Zr-Si	Zr-Zr		
Reference ^a	2.18	2.98	3.60	-	_

^a Hazen and Finger (1979).

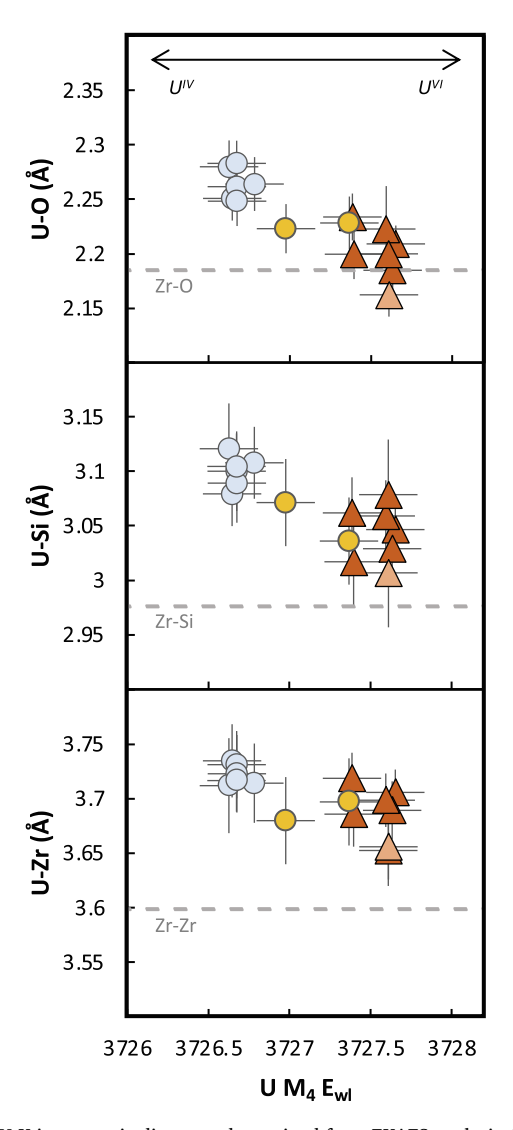


Fig. 14. U-X interatomic distances determined from EXAFS analysis. From top to bottom: U-O, U-Si, U-Zr. Dashed lines indicate the reference Zr-X distances. Symbols as in Fig. 8. (FC-1: blue circle; Ecstall: orange circle; FCT: red triangle; BT: pink triangle).

3.4. Effect of crystallographic orientation on calculated U valence

Rotation tests performed on grains mounted with their c-axis parallel or perpendicular to the polarization direction of the incident X-ray beam reveal a very limited impact of dichroism on the calculated Ewl from measured U M₄-edge spectra (Fig. 15). For the zircon grains analyzed (FCT, BT, and Ecstall), the 2 SE uncertainty in the Ewl determined for each crystal ranged from ± 0.02 to ± 0.17 eV, with an average 2 SE uncertainty of only ± 0.10 eV for these grains. For FC-1 zircon the 2 SE uncertainty was only ± 0.05 eV. The variability we observe due to crystallographic orientation is similar in magnitude to the shift observed between U-bearing compounds with different crystal structures (~0.1 eV) (Kvashnina and Butorin, 2022) and is much smaller than the differences observed between U of different oxidation states. In all cases the average deviation at each orientation is within the uncertainty of the measurement (Fig. 15c). These analyses indicate that variations in E_{wl} due to the geometry between the crystal and X-ray beam are minimal compared to the magnitude of the peak shifts between different U oxidation states. Although crystallographic orientation does not appear to be a significant source of uncertainty, we recommend that spectra be collected for multiple grains from a sample when possible.

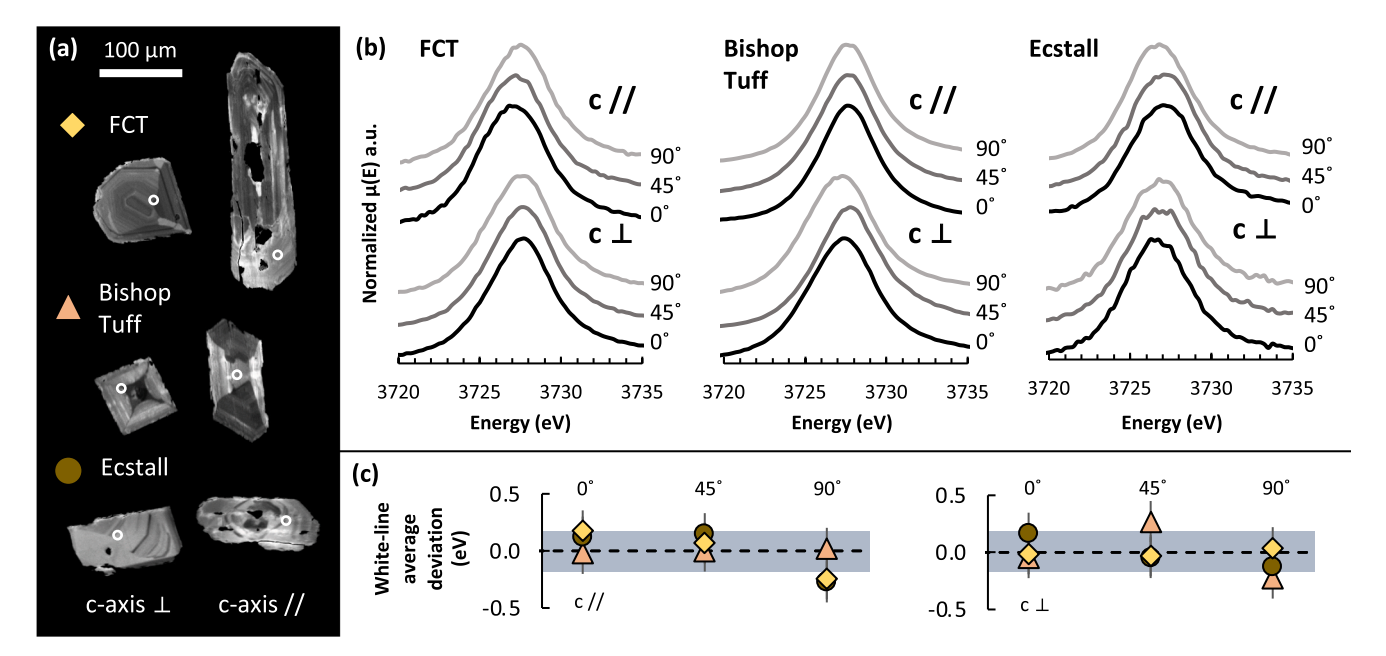


Fig. 15. (a) CL images of grains analyzed to test the effect of crystallographic orientation on U M_4 -edge spectra. The right column are the grains mounted with their c-axis approximately parallel to the mount surface. White circle shows the location of the analysis spot. Image shows grains in the 0° orientation. (b) Spectra for FCT, Bishop Tuff, and Ecstall zircons collected at each orientation. (c) Average deviation from the mean white-line energy for each grain measured at each orientation. Symbols for each sample are shown in (a) FCT: yellow diamonds; Bishop Tuff: pink triangles; Ecstall: brown circles. Colored bar represents the ± 0.18 eV uncertainty (2 SD) of the white-line energy.

3.5. Impact of radiation damage on calculated U valence

To assess the impact of radiation damage on U valence in zircon (due to decay of radioactive elements within the zircon grains), we compare the Raman peak width (E_g band) and average U valence in our samples (Fig. 16). Amongst the zircon grains investigated here, those from the FCT, Ecstall pluton, BT, Lassen, and the Sierra Nevada Plutons have Raman spectra consistent with crystalline zircon (*i.e.*, Raman peaks <10 cm⁻¹ in width). In contrast, grains from four samples (FC-1, HL-17-2, Harney Peak, and Sturgeon Lake) have peak widths between 10 cm⁻¹ and 30 cm⁻¹ indicating various degrees of radiation damage. No clear

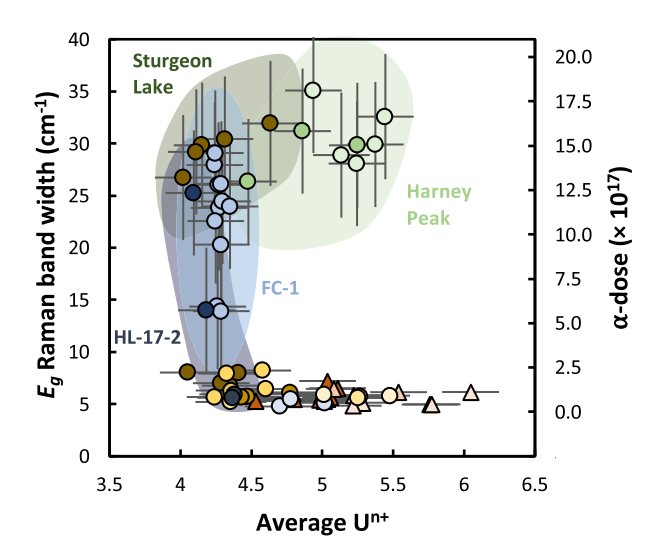


Fig. 16. Raman peak width/ α -dose vs. average U valence. α -dose calculated using the method of Härtel et al. (2022). Symbols are the same as in Fig. 7. Horizontal error bars are the 2 SD uncertainty on the U valence (± 0.2 eV), vertical error bars are the average 2 SD uncertainty of the Raman peak width (6 cm $^{-1}$ for grains with peak width > 10 cm $^{-1}$ and 0.4 cm $^{-1}$ for grains with peak width < 10 cm $^{-1}$). Symbols as in Fig. 8.

relationship between U^{n+} and Raman peak width is visible in the data. FC-1 zircon grains, while ranging from mostly crystalline to heavily radiation damaged, show no resolvable change in their U valence as a function of Raman peak width. Harney Peak zircon (HP44A and HP21C) have Raman peak widths $>25~{\rm cm}^{-1}$ and cover a range of valence states, but the two quantities appear uncorrelated. Sturgeon Lake zircon (SP-16-52) show a slightly positive trend with more reduced grains having a narrower Raman peak width. However, the Raman peak widths are all within uncertainty of each other, and this trend is thus inconclusive regarding the effect of radiation damage on U oxidation states in these crystals. Finally, zircon grains from sample HL-17-2 show a somewhat negative trend with more radiation damaged grains containing a greater proportion of U^{IV} .

4. Discussion

4.1. Effect of radiation damage on Uzrc oxidation states

Radiation damage is a persistent concern for any zircon investigation method. The decay of radioactive elements, primarily U and Th, in zircon damages the crystal lattice and over time can destroy the short to medium range order of the mineral (e.g., Farges and Calas, 1991; Nasdala et al., 1995). The time for radiation damage to accumulate to the point where the crystal becomes amorphous or unsuitable for analysis depends on the concentration of radioactive elements and can vary from millions to billions of years. These damaged zones are more susceptible to chemical alteration and can lead to spurious results when not accounted for. Specifically for U speciation, previous work has suggested that heavily radiation damaged zones in zircon may contain a greater proportion of U^{IV} relative to higher valence states (Zhang et al., 2003).

Our data show that crystalline zircon grains can have average U valences that span the entire range from U^{IV} to U^{VI} , a feature indicating that the measured U oxidation state is a primary signature, and that zircon can incorporate U of any valence during crystallization. As seen on Fig. 16, grains with varying degrees of radiation damage display a similar range of U^{n+} as crystalline grains, suggesting that they have largely retained their primary U valence state. Examination of grains

from the same sample further strengthen this interpretation. For instance, FC-1 zircon grains, which range from mostly crystalline to heavily radiation damaged, show unresolvable change in U valence as a function of Raman peak width, indicating that even high degrees of radiation damage did not significantly alter the U redox state of FC-1 zircon. Additional evidence comes from the highly radiation damaged grains (Harney Peak and Sturgeon Lake zircon) that have Raman peak widths >25 cm⁻¹. Despite their clear radiation damage Harney Peak zircon (HP44A and HP21C) display no significant trend in Fig. 16 and cluster near a predominately UV composition. Sturgeon Lake zircon (SP-16-52) show a slightly positive trend with more reduced grains having a narrower Raman peak width. However, given the large uncertainty associated with highly radiation damaged grains (6 cm⁻¹ 2 SD) this trend is inconclusive regarding the effect of radiation damage on U oxidation states in these crystals. Overall, radiation damage does not seem to have a reducing effect on the U oxidation state of the grains studied here, despite the old age and high degree of radiation of some samples (e.g., Harney Peak ~1700 Ma; Sturgeon Lake ~2670 Ma). If the U valence composition of the Harney Peak or Sturgeon Lake zircon grains have been altered, it is more probable that U has been oxidized during to fluid alteration, rather than reduced as a result of electron capture during radioactive decay as proposed by Zhang et al. (2003). This, however, is unlikely for the Harney Peak zircon as their host-rocks appear to have experienced little post-crystallization fluid alteration (Nabelek et al., 1992).

In our dataset, zircon grains from only one sample, HL-17-2, show a decrease in U valence with increasing Raman peak width. At first glance, this observation is consistent with the idea that more metamict grains may contain greater proportions of U^{IV}. However, the HL-17-2 zircon grains with more radiation damage also contain significantly more U than crystalline grains (1000s vs. 100s of ppm U), which needs to be considered. XANES analysis and Raman spectroscopy was conducted on four zircon grains from sample HL-17-2 with U concentrations varying from \sim 200–5000 ppm. In these grains, the proportion of U^{IV} and the width of features present in their Raman spectra both increase with increasing U concentration, ranging from highly radiation damaged and entirely U^{IV} to crystalline with an average valence of U^{4.4+}. Rather than radiation damage, the reduced nature of the high-U grains could simply be a result of U ion partitioning in zircon as experiments under varying redox conditions have showed that U^{IV} is more compatible in zircon than U^V or U^{VI} (Burnham and Berry 2012). When the $U_{zircon}/U_{whole\ rock}$ ratio of the individual HL-17-2 zircon are plotted against their U valence (Fig. 17), a strong negative trend is observed from high-concentrationlow-valence U to low-concentration-high-valence U. As a comparison the Uzircon/Uwhole rock ratio of samples SNB-14-34 and SNB-16-12, also from the HLMC, are plotted on Fig. 17. For the HL-17-2 zircon, the

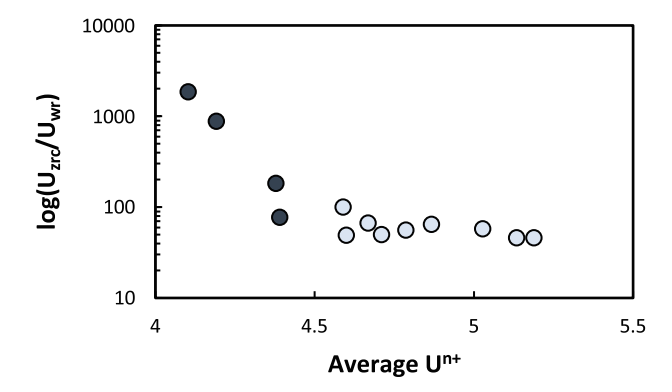


Fig. 17. Uranium partitioning between zircons and host rock for HLMC samples HL-17-2 (anorthosite, dark blue circles) and SNB-14-34 and SNB-16-12 (monzodiorites, light blue circles). The U valence of HL-17-2 zircons decreases systematically with increasing U concentration indicating a preference for U^{IV} over $U^{V/VI}$ in the zircon structure.

concentration of other incompatible elements (e.g., Hf, Y, REE) are also greater in the high-U grains suggesting the melt from which they crystallized was generally more enriched. Together, this suggests that the greater proportion of U^{IV} in the grains with higher U concentration is likely a primary signature resulting from a combination of U ion partitioning behavior and melt composition, and thus, may reflect crystallization of these grains under different conditions rather than a change in their U oxidation state due to metamictization. This is plausible for the HL-17-2 zircon as they were separated from an anorthosite block within the HLMC (Lewis et al., 2021) and zircon crystallization could have occurred in isolated melt pockets interstitial to the cumulate plagioclase grains, which could explain the variability observed in their U valence and TREE signatures. As a final indication that the trend of the HL-17-2 zircon in Fig. 16 is not due to metamictization, their behavior can be contrasted with the much older FC-1 zircon grains (95.7 Ma vs. 1099 Ma, respectively), which show little variation in U redox state (average valence of U^{4.29+}), regardless of their extent of radiation damage.

In summary, our data do not preclude the possibility that highly damaged zircon grains could have their U valence states altered, particularly if they have become entirely amorphous, as such grains give spurious results using other *in-situ* zircon methods. Our results, however, show that radiation damage has a minimal effect (within uncertainty) on the U valence determined from U M_4 -edge XANES spectra.

4.2. Incorporation of multi-valent U in zircon and U-bearing accessory phases

Our results show that zircon, apatite, and baddeleyite all may incorporate U of variable valence. Raman spectroscopy on the zircon samples shows that crystalline grains (those with Raman peak widths less than 10 cm⁻¹) have average U valences that span the entire range from U^{IV} to U^{VI}, implying that the measured U oxidation state in these zircon grains is a primary signature and that zircon can incorporate U of any valence during crystallization. In contrast to zircon and the other accessory phases investigated, titanite seem to have invariant U valence containing only the reduced species, U^{IV}. Previous work on experimentally grown titanites concluded that U incorporation was greatest in the starting media with the highest Mg concentrations, which these researchers attribute to a coupled substitution in which U replaces Ca while Mg substitutes into an adjacent octahedral site to balance the higher charge of the U atom (Tiepolo et al., 2002; Mazdab, 2009). Given its specificity, the charge balance requirements of this coupled substitution reaction would be highly unfavorable towards incorporation of oxidized uranium into titanite, regardless of melt oxidation state, which is consistent with our results.

In zircon, U is thought to substitute for Zr in the crystal structure, and thus, it is often assumed that only U^{IV} is incorporated into zircon as Zr is strictly tetravalent. However, along with U, zircon incorporates many other trace elements including yttrium (Y) and REE, which are predominantly trivalent and may provide a charge balancing mechanism for U of higher valence states (Vance and Mackey, 1974), though charge compensation may be accommodated by vacancies as well. Experimental studies have shown that the partition coefficient for uranium substitution into zircon decreases with higher melt oxidation states suggesting a preference for reduced over oxidized U in the zircon structure (Burnham and Berry, 2012). Despite a preference for U^{IV}, zircon seems able to readily incorporate U of any valence state. For example, zircon from the Bishop Tuff typically have elevated U concentrations ranging from ~800-5000 ppm and contain some of the highest proportions of oxidized U amongst our samples. This is likely due to the incompatible nature of U that results in evolved magmas (and the zircon which crystallize from them) having generally higher U concentrations compared to more primitive melts regardless of U oxidation state. While experimental studies of lab-grown zircon have not detected an appreciable amount of UVI in samples grown under oxidizing conditions, this could be due to the volatile nature of hexavalent U,

which can be easily lost from 1 atm experiments (Burnham and Berry, 2012). Our study of natural samples unambiguously shows that zircon can incorporate penta- and hexavalent U in addition to the tetravalent form. Notably, while some individual zircon grains appear to have an entirely $\boldsymbol{U}^{\text{IV}}$ composition, the lowest average \boldsymbol{U} valence calculated for a sample is $U^{4.25+}$, indicating that the incorporation of multivalent U is a common feature of zircon. The factors determining the proportions of U^{IV}, U^V, and U^{VI} in a zircon containing multivalent U are currently unconstrained, however, it is likely a result of the P-T-X conditions of the crystallizing melt. For example, the stability field of UV has been shown to decrease at higher pressures (Halse, 2014), which would result in a greater proportion of UVI in the melt relative to UV for the same degree of oxidation. While various factors likely play a role in the oxidation path of U, the proportion of oxidized U (either U^V or U^{VI}) has been shown to increase as a function of fO_2 in silicate melts (Halse, 2014) and zircon (Burnham and Berry, 2012).

4.3. U valence as a probe of magma fO2

The ability of zircon to incorporate U of any valence raises the question of what determines the valence of U in zircon. Redox conditions in the zircon parental magma are likely to exert a first-order control on U speciation in zircon. In fact, zircon grains from samples with independent fO_2 estimates display a strong positive correlation between their calculated U valence (i.e., E_{wl} of their U M₄-edge spectra) and oxygen fugacity (Fig. 18), highlighting the potential for U valence in zircon to be an accurate oxybarometer for igneous systems. The fO_2 values for samples used in this correlation were calculated from a variety of methods and include rocks of diverse lithology, illustrating the robustness of U M₄-edge spectroscopy as a tool for probing magma redox. References and methods used for each fO_2 estimate are given in Table 5 and are outlined in the following paragraph.

The fO2 values for FC-1, FCT, and LF042-02 were calculated using Fe-Ti oxide pairs by Pasteris (1985), Johnson and Rutherford (1989), and Underwood et al. (2012), respectively. For the Bishop Tuff, fO₂ estimates vary from an average of FMQ+1.1 (Hildreth and Wilson, 2007) to FMO+2.4 (Trail et al., 2011, 2012). We use the value of Trail et al. (2012) for our calibration, however, as the value determined using Fe-Ti oxide pairs for the Bishop Tuff was shown to be unreliable by Ghiorso and Gualda (2013) due to the disequilibrium growth of ilmenite just prior to, or during, eruption and thus does not reflect pre-eruptive conditions within the magma chamber. Modeling in alphaMELTS using whole rock geochemistry and biotite Fe-Mg compositions by Bucholz et al. (2018) were used to calculate fO₂ values for the SPG samples (HP21C, HP44A, SP-16-52). This method was also used for sample SNB-16-9 from the HLMC (Lewis et al, 2021). For samples HP44A and SP-16-52 the average value determined using this method was used for our calibration, however, the values predicted for sample HP21C were poorly defined (from FMQ-1.4 to FMQ+1.1), so the maximum value was used instead. For comparison, the minimum value determined for sample HP44A, also from the Harney Peak granite, was FMQ+1.45. The fO_2 of the Ecstall pluton was estimated to be FMQ+1 ± 1 based on the occurrence of titanite, which typically only forms at elevated oxygen fugacities (Xirouchakis and Lindsley, 1998; Loucks

In Fig. 18a, the data were fit using a linear approximation (Equation (3)) to provide an empirical relationship between U M_4 -edge E_{wl} and the fO_2 of a sample:

$$\Delta FMQ = \frac{(E_{wl} - E_{FMQ=0})}{slope} \tag{3}$$

where E_{wl} is the white-line energy of the spectra (in eV). Since measured E_{wl} values can vary slightly between beamlines, the E_{wl} of FC-1 zircon can be used as a reference to define $E_{FMQ=0}$ in Eq. (3), and ΔFMQ values can be calculated from the difference between the E_{wl} of FC-1 zircon and

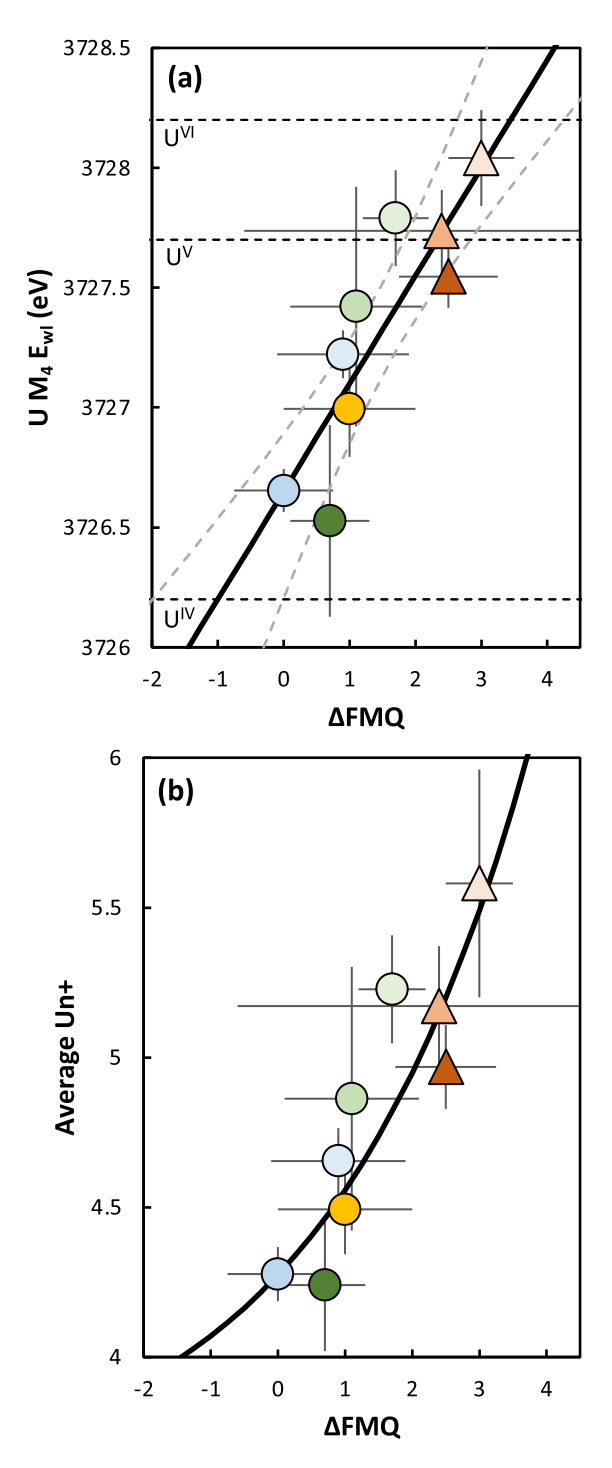


Fig. 18. Variation in oxygen fugacity relative to the FMQ buffer with (a) U M_4 E_{wl} and (b) average U^{n+} . Vertical error bars are the 2 SE for each sample. Horizontal error bars are from the published fO_2 estimates given in Table 5. Dashed line in (a) shows the 95 % confidence interval of the fit. Symbols as in Fig. 8.

the unknown. For the beamline used in this work (APS 13-ID-E), the best fit takes the form:

$$\Delta FMQ = \frac{(E_{wl} - 3726.65)}{0.45} \pm 1.0(2\sigma) \tag{4}$$

A linear approximation provides a good fit to the data; however, it is expected that below a particular fO_2 all U in zircon would be present as entirely U^{IV} and above a particular fO_2 all U would be present as U^{VI} . As

Table 5
White-line energy, fO₂ estimate, method of fO₂ determination, and references used for calibration of the U M₄-edge XANES oxybarometer in Fig. 18.

Sample	White-line (eV)	ΔFMQ	Method	Reference
LF042-02	3728.04	3.0 ± 0.5	Fe-Ti oxides	Underwood et al. (2012)
BT	3727.74	2.4 ± 3.1	Ce in zrc	Trail et al. (2011, 2015)
FCT	3727.55	2.5 ± 0.8	Fe-Ti oxides	Johnson and Rutherford (1989)
HP44A	3727.79	1.7 ± 0.5	Biotite Fe-Mg modeling	Bucholz et al. (2018)
HP21C	3727.42	1.1 ± 1.0	Biotite Fe-Mg modeling	Bucholz et al. (2018)
SNB-16-9	3727.22	0.9 ± 1.0	Biotite Fe-Mg modeling	Lewis et al. (2021)
Ecstall	3726.99	1.0 ± 1.0	Petrology	estimate (titanite present)
SP-16-52	3726.53	0.7 ± 0.6	Biotite Fe-Mg modeling	Bucholz et al. (2018)
FC-1	3726.65	0.0 ± 1.0	Fe-Ti oxides	Pasteris (1985)

To maintain consistency, published fO₂ values were recalculated as deviations from the fayalite-magnetite-quartz buffer (ΔFMQ) when necessary.

such, this model is only able to predict Δ FMQ values within this interval. From Equation (4) and the approximate edge energies of the various U valence states (Fig. 8), the range of fO_2 values over which this model is applicable is FMO-1 to FMO+3.5. These values correspond to 3726.2 eV and 3728.2 eV, which are the energies determined for the UIV and UVI edges, respectively. It should be noted, however, that the lowest and highest white-line energies of individual zircon grains are slightly below and above these values (at 3726.0 \pm 0.18 eV and 3728.3 \pm 0.18 eV; Fig. 8) but are within uncertainty of the nominal edge energies for U^{IV} and $\mathbf{U}^{\overline{VI}}$. These slight differences in energy may arise due to crystallographic effects, which can lead to variations in white line energy on the order of \sim 0.1 eV (Fig. 15). As such, zircon with white-line energies less than the nominal U^{IV} E_{wl} (3726.2 eV) or greater than the U^{VI} E_{wl} (3728.2 eV) should be treated as having crystallized at an oxygen fugacity equal to or below FMQ-1 or equal to or above FMQ+3.5, respectively. Importantly, while this approach can only predict Δ FMQ values over a limited range, the interval over which this model is valid encompasses the expected redox states of most zircon-bearing magmas. Should U valence be determined using a different technique (for example U L3-edge XANES), a more general formalism, relating U valence in zircon to $\Delta FMQ,$ would be useful. Such a relationship is provided in Equation (5) below (see Fig. 18b):

$$\Delta FMQ = 3.07 \ln \left(\frac{U^{n+} - 3.54}{0.53} \right) - 1 \tag{5}$$

Having thus calibrated the system, we then use Eq. (4) to calculate fO_2 values for the zircon samples for which no robust oxygen fugacity estimates were available. The minimum and maximum ΔFMQ values calculated for zircon grains from each of these samples are given in Table 6. Since the variation between E_{wl} and ΔFMQ in our model is

Table 6 fO_2 values of zircon samples* calculated using Eq. (3).

Sample		ΔFMQ	ΔFMQ
		min	max
Long Valley Caldera			
MC18-2	n = 3	+3.1	>+3.5
MC18-4	n = 2	+3.3	>+3.5
Sierra Nevada			
Bullfrog Pluton	n = 3	+2.1	+3.0
Dragon Pluton	n=2	+0.3	+2.6
Independence Pluton	n = 4	-0.1	+1.1
Whitney Intrusive Suite			
Mt. Whitney granite	n = 1	+0.3	+0.3
Lone Pine granodiorite	n=2	-0.01	+0.04
Paradise granodiorite	n=4	-1	+0.5
Hidden Lakes Mafic Complex			
SNB-16-12	n = 5	+1.4	+2.5
SNB-14-34	n=4	+1.1	+1.8
SNB-16-6	n=4	+0.5	+1.4
SNB-14-40	n = 7	-0.2	+ 0.6
HL-17-2	n=4	-0.9	+0.4
TEM2	n=2	+0.1	+0.3
Dariv Igneous Complex	n = 26	-0.5	+0.5
91500/KL	n=6	0	+0.5
Pacoima Pegmatite	n = 4	-1.0	+0.6

^{*} Samples used for calibration of Eq. (3) are excluded.

linear, the relative difference in fO_2 between samples is similar to the differences in E_{wl} shown in Fig. 8. For example, zircon from the Long Valley Caldera (MC18-2 and MC18-4) have the highest E_{wl} values amongst our samples, with spectra indicative of an almost entirely U^{VI} composition and return fO_2 values at the upper limit of our model (FMQ+3.5). On the low end, zircon from the syenite samples (91500/KL and Pacoima Pegmatite) return fO_2 values of \sim FMQ and have an average valence of $U^{4.3+}$. We note that our fO_2 estimate for the 91500 zircon (FMQ to FMQ+0.5) is greater than the estimate of Loucks et al. (2020) (FMQ-1.4), however, in their model U is assumed to occur almost entirely in the tetravalent state, which we have shown is not the case for this sample. Modification of the Loucks et al. (2020) model to account for a greater proportion of oxidized U in 91500 zircon would result in an increase in the predicted fO_2 , bringing our estimates into better agreement.

The oxygen fugacity values we determine for suites of related rocks reveal interesting differences in the redox behavior of these systems. Samples from the DIC (Bucholz et al., 2014, 2017) have tightly clustered white-line energies and range from FMQ-0.5 to +0.5 for this sample suite as a whole (n = 26). This result is striking as the Dariv zircon were separated from diverse lithologies within the complex, including monzonites, a lamprophyre dike, and a felsic dike. Samples from the Whitney Intrusive Suite in the southern Sierra Nevada (Table 6) also show similar redox states (FMQ-0.01 to +0.5, excluding one outlier at FMQ-1) despite differences in composition and crystallization conditions (Hirt, 2007). The similar fO_2 amongst samples from these two suites suggests that the redox state of these magmas underwent little change during their emplacement and subsequent differentiation. In contrast, zircon samples from the HLMC (Lewis et al., 2021) record markedly different magma redox states between samples, ranging from FMQ-0.9 to +0.4 for the most reduced sample (HL-17-2), to FMQ+1.4 to +2.5 for the most oxidized sample (SNB-16-12). The HLMC samples also show a >1 log unit difference between the average fO_2 of the cumulate (FMQ+0.1) and liquid-like (FMQ+1.4) samples indicating evolving redox conditions within the HLMC. Overall, the fO2 values we determine for the HLMC agrees well with the estimate of Lewis et al. (2021) for these rocks of \sim FMQ+1 \pm 1. While a thorough investigation into the redox behavior of these systems is beyond the scope of this study, these observations present a compelling direction for future work.

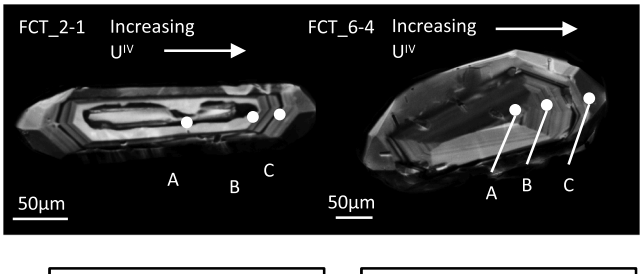
A potential complication to using U valence in zircon as a magma redox proxy is the variable partitioning behavior of U between zircon and melt, as $D_{U(IV)} > D_{U(V)} > D_{U(V)}$, where $D_{U(i)}$ is the zircon-melt partition coefficient (Burnham and Berry, 2012; Mallmann et al., 2021). While the relationship between U valence and $D_{U(i)}$ warrants further exploration, in most cases the effect of differential partitioning between U ions on the estimated fO_2 should be minimal. Since U is a trace element in most igneous systems, its oxidation state should be buffered by the more abundant redox sensitive species (e.g., Fe, C-O-H-S gasses/liquids), leading to a consistent U valence recorded by zircon for a given oxygen fugacity. However, in the case of zircon crystallization from small degree partial melts or low volumes of residual melt, the preferential uptake of U^{IV} may lead to an underestimation of fO_2 if the redox state of melt is not buffered (i.e., the system is not in equilibrium).

As an incompatible element, U concentrations in low degree melts are typically high, leading to correspondingly high concentrations of U incorporated into zircon. Thus, we recommend that care be taken when applying the U M_4 XANES oxybarometer to zircon with exceptionally high U concentrations (e.g., >2000 ppm).

Our results show that U valence in zircon is a powerful proxy for magma redox. Given the near ubiquity of zircon in evolved igneous rocks and their extreme resistance to alteration, the use of U XANES to extract information on magma redox from zircon opens a new way of interrogating the rich zircon record that will allow for the fO_2 of crustal rocks to be reconstructed throughout most of Earth's history.

4.4. Intra-grains variations in U M₄-edge spectra

The concentrations of uranium and other trace elements are known to vary within different growth zones of the same zircon crystal due to evolving conditions in the crystallizing melt. The small analytical spot size (1-5 µm) of XANES measurements enables probing of individual growth zones within a zircon crystal and thus allows for their interrogation on an intra-grain level. To explore how U oxidation state can vary within a single zircon, measurements were made at several points across individual FCT zircon grains as these crystals typically have complex growth patterns and oscillatory zonation in CL images. Analysis locations and their corresponding spectra for two FCT grains are shown in Fig. 19. Across these transects both crystals show a decrease in U oxidation state from the core to the rim of the crystal. While zircon FCT 2-1 in Fig. 19 contains an antecrystic (or xenocrystic) core analyzed at point A (which may not reflect conditions of the erupted Fish Canyon Tuff liquid), a general rim-ward decrease in Uⁿ⁺ is observed amongst most of the FCT zircon analyzed in this study. Fig. 20a shows the average U valence of individual spot locations plotted against the location of the analysis point for five FCT and eight FC-1 zircons. The location is plotted as the fractional distance of the measurement point along a line from the



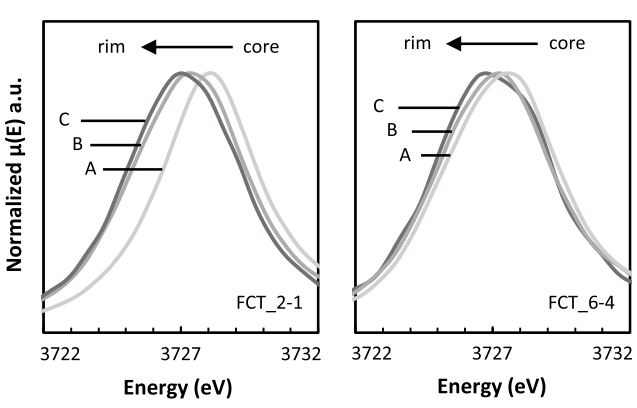


Fig. 19. CL images for two FCT zircons and their corresponding spectra collected along a transect parallel to the c-axis. Both crystals show a rim-ward decrease in white-line energy.

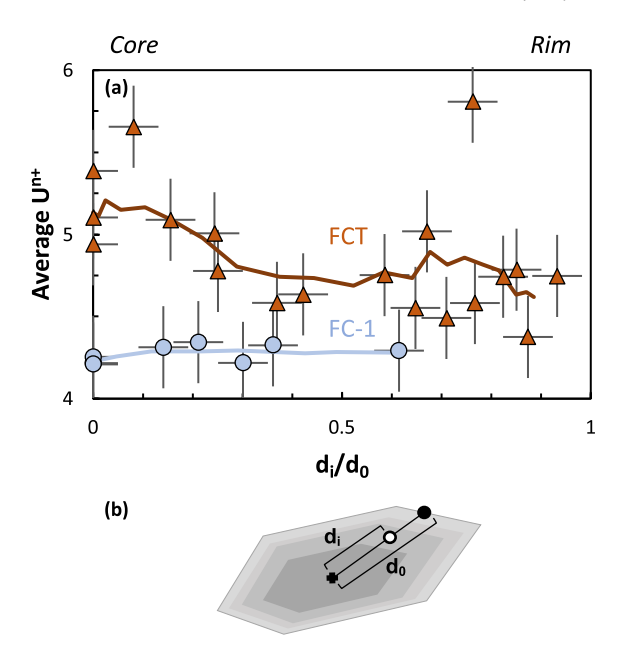


Fig. 20. (a) Variation in U valence for FCT and FC-1 zircon plotted against the fractional distance from the approximate center of the grain. Only FCT samples with multiple spot locations are shown. Solid lines are the moving average of the data points (n = 5). (b) Cartoon illustrating formulation of the fractional distance plotted in (a).

center of the grain to the edge of the crystal (Fig. 20b). This quantity is used to serve as a rough approximation of the zircon growth stage that each analysis targeted. From the core rim-ward, FCT zircon show a general decrease in average U valence, although there is an increase in variability at the grain rims. FC-1 zircons on the other hand, appear homogenous in CL images and likewise show little variation in \mathbf{U}^{n+} with distance from the center of the grain. The spread in U oxidation states at FCT grain edges may be the result of sampling zircon that completed their growth at different stages of magmatic evolution, or which completed their growth in different locations within the magma chamber if the entire melt was not in equilibrium. For example, grains with a greater abundance of oxidized U at their margins could have grown from a melt which had interacted with oxidizing fluids in the near surface just prior to or during eruption. During the main stage of zircon growth, however, the parental melt to the FCT zircon grains appears to have been evolving towards a more reduced state. Cottrell et al. (2021), and references therein, show that degassing of a C-O-H-S vapor from a magma chamber can lower fO_2 and may explain the general rim-ward decrease in U oxidation state observed in FCT zircons. There is still much to be explored regarding intra-grain variations in U oxidation states and the possible driving mechanisms, but this exercise shows that U XANES can be used to gain insight into the crystallization history of single zircon grains and can elucidate redox changes occurring within an individual magma body during its evolution.

4.5. Variation in U valence between coexisting phases

Samples with coexisting U-bearing accessory phases show differences in the U valence of the different minerals. Minerals from the FCT show the greatest variability between phases with E_{wl} varying across 1.25 eV from 3727.55 eV (\sim U⁵⁺) for zircon to 3726.3 eV (entirely U^{IV}) for titanite, while the E_{wl} of apatite is intermediate at 3726.9 eV (Fig. 21). Zircon and baddeleyite from FC-1 are also distinct in their peak

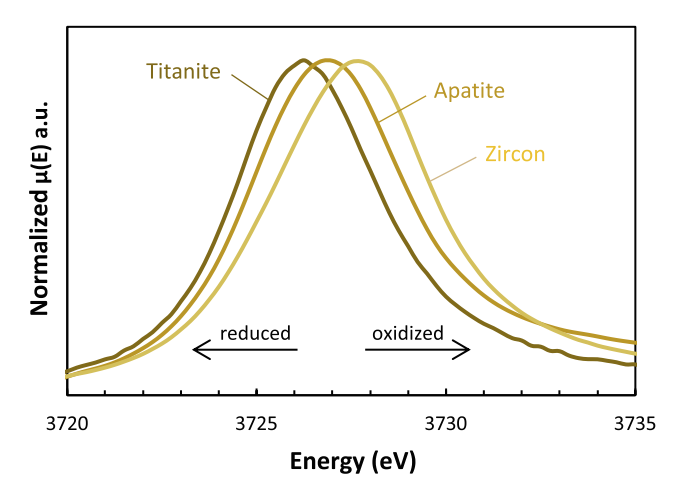


Fig. 21. Average U M_4 -edge spectra for titanite, apatite, and zircon from Fish Canyon Tuff.

positions with baddeleyite having a slightly higher proportion of oxidized U relative to zircon (Fig. 8). The variability in white line energy observed between zircon and coexisting apatite or baddeleyite may either reflect a preference for a particular U oxidation state in these minerals (similar to titanite incorporating only reduced U), or crystallization of these phases during different stages of magmatic evolution. One possibility, for instance, would be that early crystallization of titanite, which only incorporates UIV, could modify the average U valence of the parental melt, and thus that recorded by the zircon. A simple mass balance calculation, however, shows that this hypothesis is unlikely. For instance, FCT samples contain ~0.5 % titanite, with titanite and whole rock U concentrations of 50–100 ppm and 4–5 ppm, respectively (Bachmann et al., 2002; Schmitz and Bowring, 2001). This means that only between 5 % and 12.5 % of the total U content in the rock is hosted by titanite, a value too small to have a noticeable effect on the valence of U incorporated into FCT zircon (at our current level of precision). Furthermore, if titanite crystallization were to exert a control on the U valence recorded by FCT zircon it would be expected to lower the proportion of UIV and lead to progressively higher valence U incorporated into zircon as crystallization progresses (assuming cocrystallization of these phases). However, an opposite trend is observed in the FCT, with E_{wl} decreasing from the core rim-ward for most zircon grains (Fig. 19). As a trace element, U concentrations in crustal rocks are low, generally between 1 and 10 ppm, and thus, its redox state may be buffered by more abundant species (e.g., Fe, H_2O , and C-O-H-S gasses) if only a particular oxidation state is removed during crystallization. While the impact of titanite crystallization on U valence in zircon appears minimal for the FCT, this may not be the case for all samples. For example, if zircon and titanite co-crystallize within isolated melt pockets or from low-degree partial melts, titanite may impart a stronger effect on zircon U valence. As such, future work examining the relationship between U valence in these phases from a more diverse set of lithologies should be undertaken.

4.6. Implications for U isotope fractionation

Solution measurements of $^{238}\text{U}/^{235}\text{U}$ in pooled zircons fractions (100s-1000s of single crystals) (Hiess et al. 2012, Livermore et al., 2018) and single grains (Tissot et al., 2019) show variability in $\delta^{238}\text{U}$ of \sim 0.6 ‰, with even greater fractionations (up to 4.8 ‰) between zircon and titanite from the same sample. Laser ablation MC-ICPMS data show a

similar spread in zircon, and an even larger range in titanite, from -3.5 \pm 2.2 % to +13.1 \pm 3.4 % (Yamamoto et al., 2021). These variations indicate the presence of significant uranium isotope fractionations during magmatic processes, whose origin are currently unconstrained. For heavy elements such as uranium, equilibrium isotope fractionations can be driven by: 1) difference in coordination environments, for instance between crystals and melt, with heavy isotopes concentrating where coordination numbers are low and valence is high, or 2) changes in the size and shape of the atomic nucleus between odd and evennumbered isotopes, known as the nuclear field shift effect, resulting in isotopes with odd numbers of neutrons behaving as if they had a smaller mass, which for U leads to preferential incorporation of heavy isotopes in reduced species (Bigeleisen, 1996a, 1996b). While the magnitude of the effects seen in titanite almost certainly indicates a kinetic origin for some U isotope fractionations (Tissot and Ibañez-Mejia, 2021), the more subtle variations seen in zircon could be redox driven. As such, future work performing coupled investigation of U-isotope fractionation and U speciation in zircon from different samples and between zircon and coexisting accessory phases may help elucidate the driver of hightemperature U-isotope fractionation.

5. Concluding remarks

We conducted a systematic investigation of the oxidation state of uranium in several important U-bearing accessory phases using U $\rm M_4$ -edge XANES. The data (Figs. 6–8) reveals that zircon, apatite, and baddeleyite can contain multivalent uranium, while titanite contains only $\rm U^{IV}$. The garnet samples investigated herein also appear to only contain $\rm U^{IV}$, but this may not be the case for all types of garnet as only two grains of similar composition were analyzed. Of the minerals we investigated, zircon shows the greatest variability in the proportions of the different U oxidations states it can incorporate, with spectra indicative of nearly pure $\rm U^{IV}$, $\rm U^{V}$, and $\rm U^{VI}$ compositions as well as mixtures of these species.

The potential effects of systematic biases on zircon U M₄-edge white-line energies were investigated. Repeat measurements on the same spot shows that beam damage does not affect U oxidation states in zircon (Fig. 5), while rotation tests indicate that crystallographic effects (i.e., sample orientation) have a minimal effect on the measured E_{wl} of U M₄-edge spectra (Fig. 15). Similarly, comparison of Raman peak width vs. zircon U^{n+} indicates that radiation damage also has little effect on U M₄-edge spectra (Fig. 16). Instead, our results show that the U M₄-edge E_{wl} (and U^{n+}) of zircon samples is strongly correlated with the parental magma fO_2 , indicating that U oxidation states in zircon as determined by XANES can be used as a tracer of magma redox (Fig. 18). The preferential partitioning of reduced U over oxidized U in zircon (i.e., $D_{U(IV)} > D_{U(V)} > D_{U(V)}$), while potentially a limitation of the method, does not seem to have any significant effect on fO_2 estimates in typical zircon grains (i.e., with U content < 1000 ppm).

This new approach has several advantages over other zircon-based oxybarometers that use Ce and other trace element concentrations to infer magma redox states (e.g., Trail et al. 2011; Smythe and Brenan, 2016; Loucks et al., 2020). First, the concentration of trace elements in zircon can vary due to a variety of factors other than oxygen fugacity, such as melt composition and temperature (e.g., Zou et al., 2019; Loader et al., 2022). In particular, Loader et al. (2022) showed that increases in Ce-anomalies, which form the basis of several zircon oxybarometers, can occur due to cooling at constant fO_2 or due to the presence of certain cocrystallizing phases. Second, these methods can rely on difficult to constrain parameters such as the activity of H_2O or melt polymerization (e.g., Smythe and Brenan, 2016). Third, they often require the composition of the melt be known or estimated from whole rock compositions

(Trail et al., 2011; Smythe and Brenan, 2016). Lastly, the oxidation state of U is assumed to be exclusively tetravalent in the model formulations of the Smythe and Brenan (2016) and Loucks et al. (2020) oxybarometers, which we show here is not the case, leading to a misestimation of fO2 for zircon containing oxidized uranium. XANES, on the other hand, is a direct measure of an element's oxidation state and should be more closely related to melt fO2 compared to element concentrations. Since U is typically present in sufficient amounts to produce reliable spectra for most zircon crystals (100s of ppm or more), this technique is widely applicable to most zircon-bearing lithologies and even single detrital zircon crystals. Furthermore, U XANES does not necessitate knowledge of the host rock composition, so this approach could be particularly useful for studies of zircon that have been removed from their original context, such as in detrital settings. Additionally, the small analytical spot size (<2 µm) and non-destructive nature of XANES make this method amenable to investigating magma redox changes within individual zircon growth zones and allows this technique to be used in conjunction with other in situ zircon methods (e.g., LA-ICPMS, SIMS). In summary, U M₄-edge XANES analysis of zircon can provide a reliable and straightforward method for interrogating magma redox conditions from the global scale to that of a single pluton or eruption, and throughout Earth's history from the Hadean to the present.

Data availability

Data are available through Caltech Data at: https://doi.org/10.22002/36sg9-yhj98.

Declaration of competing interest

The authors declare that they have no known competing financial interests or personal relationships that could have appeared to influence the work reported in this paper.

Acknowledgements

SKH thank Chi Ma for training and help with the SEM, as well as Maddie Lewis for providing zircons from the HLMC, Jade Star Lackey for providing zircons from the Sierra Nevada plutons and the garnet samples, Claire Bucholz for providing the zircons from the Dariv Igneous Complex and the SPG samples, Barbara Ratschbacher for providing rock samples of LF042-02 (Lassen) and MC18-2,4 (Long Valley Caldera), and Carl Swindle for providing rock samples of the Pacoima Canyon Pegmatite. Thoughtful comments from the associate editor, George Calas, and three anonymous reviewers helped to strengthen the manuscript. This work was supported by NSF CAREER grant EAR-2145780 to FLHT, as well as a Discovery grant and start-up funds to FLHT provided by Caltech. MIM and the Arizona LaserChron Center acknowledge support by NSF award EAR-2050246. This research used resources of the Advanced Photon Source, a U.S. Department of Energy (DOE) Office of Science User Facility operated for the DOE Office of Science by Argonne National Laboratory under Contract No. DE-AC02-06CH11357. We acknowledge the support of GeoSoilEnviroCARS (Sector 13), which is supported by the National Science Foundation - Earth Sciences (EAR-1634415).

Author contributions

FLHT and MIM conceived and initiated the project. FLHT, MIM and SKH designed the research. SKH prepared and characterized the samples. SKH, FLHT, MIM, MN, AL performed the XAS measurements. SKH and GR performed the Raman measurements. SKH, FLHT, MIM, MN, AL

analyzed and interpreted the data. SKH wrote the initial manuscript under FLHT's guidance, and with input from MIM, MN, AL and GR. FP contributed to the initial beamtime request and the first XAS session.

Appendix A. Supplementary material

The supplementary materials for this article are contained in one PDF document. This file contains μ XRF and SEM images of all analyzed mineral grains (Fig. S1), a figure showing the results of linear combination analysis of U M₄-edge spectra (Fig. S2), a figure showing all U L₃-edge spectra (Fig. S3), and a table of principal component analysis results (Table S1). Supplementary material to this article can be found online at https://doi.org/10.1016/j.gca.2024.07.032.

References

- Aleinikoff, J.N., Wintsch, R.P., Tollo, R.P., Unruh, D.M., Fanning, C.M., Schmitz, M.D., 2007. Ages and origins of rocks of the Killingworth dome, south-central Connecticut: implications for the tectonic evolution of southern New England. Am. J. Sci. 307, 63–118
- Anderson, A.J., Hanchar, J.M., Hodges, K.V., van Soest, M.C., 2020. Mapping radiation damage zoning in zircon using Raman spectroscopy: implications for zircon chronology. Chem. Geol. 538, 119494.
- Ankudinov, A.L., Ravel, B., Rehr, J.J., Conradson, S.D., 1998. Real-space multiplescattering calculation and interpretation of x-ray-absorption near-edge structure. Phys. Rev. B 58, 7565–7576.
- Bachmann, O., Dungan, M., Lipman, P., 2002. The Fish Canyon magma body, San Juan volcanic field, Colorado: rejuvenation and eruption of an upper-crustal batholith. J. Pet. 43, 1469–1503.
- Barth, A.P., Wooden, J.L., Coleman, D.S., 2001. SHRIMP-RG U-Pb zircon geochronology of mesoproterozoic metamorphism and plutonism in the Southwesternmost United States. J. Geol. 109, 319–327.
- Berry, A.J., Yaxley, G.M., Woodland, A.B., Foran, G.J., 2010. A XANES calibration for determining the oxidation state of iron in mantle garnet. Chem. Geol. 278, 31–37.
- Bigeleisen, J., 1996a. Nuclear size and shape effects in chemical reactions. Isotope chemistry of the heavy elements. J. Am. Chem. Soc. 118, 3676–3680.
- Bigeleisen, J., 1996b. Temperature dependence of the isotope chemistry of the heavy elements. Proc. Natl. Acad. Sci. 93, 9393–9396.
- Black, L.P., Kamo, S.L., Allen, C.M., Davis, D.W., Aleinikoff, J.N., Valley, J.W., Mundil, R., Campbell, I.H., Korsch, R.J., Williams, I.S., Foudoulis, C., 2004. Improved 206Pb/238U microprobe geochronology by the monitoring of a trace-element-related matrix effect; SHRIMP, ID-TIMS, ELA-ICP-MS and oxygen isotope documentation for a series of zircon standards. Chem. Geol. 205, 115-140.
- Brouder, C., 1990. Angular dependence of X-ray absorption spectra. J. Phys.: Condens Matter 2, 701–738.
- Brounce, M., Kelley, K.A., Cottrell, E., Reagan, M.K., 2015. Temporal evolution of mantle wedge oxygen fugacity during subduction initiation. Geol. 43, 775–778.
- Bucholz, C.E., Jagoutz, O., Schmidt, M.W., Sambuu, O., 2014. Fractional crystallization of high-K arc magmas: biotite- versus amphibole-dominated fractionation series in the Dariv Igneous Complex, Western Mongolia. Contrib. Min. Petrol. 168, 1072.
- Bucholz, C.E., Eddy, M.P., Jagoutz, O., Bowring, S.A., Schmidt, M.W., Sambuu, O., 2017. Constraining the time scales of magmatic differentiation with U-Pb zircon geochronology. Geol. 45, 11–14.
- Bucholz, C.E., Stolper, E.M., Eiler, J.M., Breaks, F.W., 2018. A comparison of oxygen fugacities of strongly peraluminous granites across the Archean-Proterozoic boundary. J. Pet. 59, 2123–2156.
- Burnham, A.D., Berry, A.J., 2012. An experimental study of trace element partitioning between zircon and melt as a function of oxygen fugacity. Geochim. Cosmochim. Acta 95, 196–212.
- Butler, R.F., Gehrels, G.E., Baldwin, S.L., Davidson, C., 2002. Paleomagnetism and geochronology of the Ecstall pluton in the Coast Mountains of British Columbia: evidence for local deformation rather than large-scale transport: ECSTALL PLUTON. J. Geophys. Res. 107. EPM 3-1-EPM 3-13.
- Chen, J.H., Moore, J.G., 1982. Uranium-lead isotopic ages from the Sierra Nevada Batholith, California. J. Geophys. Res. 87, 4761–4784.
- Cherniak, D.J., Hanchar, J.M., Watson, E.B., 1997. Diffusion of tetravalent cations in zircon. Contrib. Min. Petrol. 127, 383–390.
- Chew, D.M., Babechuk, M.G., Cogné, N., Mark, C., O'Sullivan, G.J., Henrichs, I.A., Doepke, D., McKenna, C.A., 2016. (LA, Q)-ICPMS trace-element analyses of Durango and McClure Mountain apatite and implications for making natural LA-ICPMS mineral standards. Chem. Geol. 435, 35–48.
- Cottrell, E., Birner, S.K., Brounce, M., Davis, F.A., Waters, L.E., Kelley, K.A., 2021. Oxygen fugacity across tectonic settings. In: Moretti, R., Neuville, D.R. (Eds.), Geophysi. Mono. Series. Wiley. pp. 33–61.
- Crowley, J.L., Schoene, B., Bowring, S.A., 2007. U-Pb dating of zircon in the Bishop Tuff at the millennial scale. Geol. 35, 1123.

- Davies, J.H.F.L., Stern, R.A., Heaman, L.M., Moser, D.E., Walton, E.L., Vennemann, T., 2018. Evaluating baddeleyite oxygen isotope analysis by secondary ion mass spectrometry (SIMS). Chem. Geol. 479, 113–122.
- Dawson, P., Hargreave, M.M., Wilkinson, G.R., 1971. The vibrational spectrum of zircon (ZrSiO₄). J. Phys. C Solid State Phys. 4, 240–256.
- Dominé, F., Velde, B., 1985. Preliminary investigation of the processes governing the solubility of uranium in silicate melts. Bull. De Min. 108, 755–765.
- Farges, F., Calas, G., 1991. Structural analysis of radiation damage in zircon and thorite: an X-ray absorption spectroscopic study. Am. Min. 76 (1-2), 60-73.
- Farges, F., Ponader, C.W., Calas, G., Brown, G.E., 1992. Structural environments of incompatible elements in silicate glass/melt systems: II. UIV, UV, and UVI. Geochim. Cosmochim. Acta 56, 4205–4220.
- Ghiorso, M.S., Gualda, G.A.R., 2013. A method for estimating the activity of titania in magmatic liquids from the compositions of coexisting rhombohedral and cubic iron-titanium oxides. Contrib. Min. Petrol. 165, 73–81.
- Gleadow, A., Harrison, M., Kohn, B., Lugo-Zazueta, R., Phillips, D., 2015. The Fish Canyon Tuff: a new look at an old low-temperature thermochronology standard. EPSL 424, 95–108.
- Halse, H., 2014. Using synchrotron radiation to determine the oxidation state of uranium in magmas. Imperial College London. PhD thesis.
- Hanchar, J.M., Hoskin, P.W.O., Mineralogical Society of America (Eds.), 2003. Zircon. Rev. Min. Geochem. Vol. 53.
- Harrison, T.M., Bell, E.A., Boehnke, P., 2017. Hadean Zircon Petrochronology. Rev. Min. Geochem. 83, 329–363.
- Härtel, B., Jonckheere, R., Ratschbacher, L., 2022. Multi-band Raman analysis of radiation damage in zircon for thermochronology: partial annealing and mixed signals. Geochem. Geophys. Geosyst. 23.
- Hazen, R.M., Finger, L.W., 1979. Crystal structure and compressibility of zircon at high pressure. Am. Min. 64 (1–2), 196–201.
- Hiess, J., Condon, D.J., McLean, N., Noble, S.R., 2012. ²³⁸ U/²³⁵ U systematics in terrestrial uranium-bearing minerals. Science 335, 1610–1614.
- Hildreth, W., 2004. Volcanological perspectives on Long Valley, Mammoth Mountain, and Mono Craters: several contiguous but discrete systems. J. Volcan. Geotherm. Res. 136, 169–198.
- Hildreth, W., Wilson, C.J.N., 2007. Compositional zoning of the bishop tuff. J. Pet. 48, 951–999
- Hirt, W.H., 2007. Petrology of the Mount Whitney Intrusive Suite, eastern Sierra Nevada, California: implications for the emplacement and differentiation of composite felsic intrusions. Geol. Soc. Am. Bull. 119, 1185–1200.
- Ibañez-Mejia, M., Gehrels, G.E., Ruiz, J., Vervoort, J.D., Eddy, M.P., Li, C., 2014. Small-volume baddeleyite (ZrO2) U-Pb geochronology and Lu–Hf isotope geochemistry by LA-ICP-MS, techniques and applications. Chem. Geol. 384, 149–167.
- Johnson, M.C., Rutherford, M.J., 1989. Experimentally determined conditions in the Fish Canyon Tuff, Colorado, Magma Chamber. J. Pet. 30, 711–737.
- Kelley, K.A., Cottrell, E., 2009. Water and the oxidation state of subduction zone magmas. Science 325, 605-607.
- Kvashnina, K.O., Butorin, S.M., 2022. High-energy resolution X-ray spectroscopy at actinide M_{4,5} and ligand K edges: what we know, what we want to know, and what we can know. Chem. Commun. 58, 327–342.
- Le Pape, P., Stetten, L., Hunault, M.O.J.Y., Mangeret, A., Brest, J., Boulliard, J.C., Morin, G., 2020. HERFD-XANES spectroscopy at the U M-edge applied to the analysis of U oxidation state in a heavily contaminated wetland soil. App. Geochem. 122, 104714
- Leinders, G., Bes, R., Pakarinen, J., Kvashnina, K., Verwerft, M., 2017. Evolution of the uranium chemical state in mixed-valence oxides. Inorg. Chem. 56, 6784–6787.
- Lewis, M.J., Bucholz, C.E., Jagoutz, O.E., 2021. Evidence for polybaric fractional crystallization in a continental arc: hidden Lakes mafic complex, Sierra Nevada batholith. California. Contrib. Min. Petrol. 176, 90.
- Livermore, B.D., Connelly, J.N., Moynier, F., Bizzarro, M., 2018. Evaluating the robustness of a consensus 238U/235U value for U-Pb geochronology. Geochim. Cosmochim. Acta 237, 171–183.
- Loader, M.A., Nathwani, C.L., Wilkinson, J.J., Armstrong, R.N., 2022. Controls on the magnitude of Ce anomalies in zircon. Geochim. Cosmochim. Acta 328, 242–257.
- Loucks, R.R., Fiorentini, M.L., Henríquez, G.J., 2020. New magmatic oxybarometer using trace elements in zircon. J. Pet. 61, egaa034.
- Mallmann, G., Burnham, A.D., Fonseca, R.Ō.C., 2021. Mineral-melt partitioning of redoxsensitive elements. In: Moretti, R., Neuville, D.R. (Eds.), Geophys. Mono. Series. Wiley, pp. 345–367.
- Marsellos, A.E., Garver, J.I., 2010. Radiation damage and uranium concentration in zircon as assessed by Raman spectroscopy and neutron irradiation. Am. Min. 95, 1192–1201.
- Mazdab, F.K., 2009. Characterization of flux-grown trace-element-doped titanite using the high-mass-resolution ion microprobe (SHRIMP-RG). Can. Min. 47, 813–831.
- Nabelek, P.I., Russ-Nabelek, C., Denison, J.R., 1992. The generation and crystallization conditions of the Proterozoic Harney Peak Leucogranite, Black Hills, South Dakota, USA: petrologic and geochemical constraints. Contibr. Min. Petrol. 110, 173–191.
- Nasdala, L., Irmer, G., Wolf, D., 1995. The degree of metamictization in zircon: a Raman spectroscopic study. Eur. J. Min. 7, 471–478.
- Newville, M., 2013. Larch: an analysis package for XAFS and related spectroscopies. J. Phys. Conf. Ser. 430, 012007.
- Newville, M., 2014. Fundamentals of XAFS. Rev. Min. Geochem. 78, 33–74. Newville, M., Ravel, B., 2020. IFEFFIT and LARCH. Int. Tab. Cryst. 1.

- Orihashi, Y., Nakai, S., Hirata, T., 2008. U-Pb age determination for seven standard zircons using inductively coupled plasma-mass spectrometry coupled with frequency quintupled Nd-YAG ($\lambda=213\,$ nm) laser ablation system: comparison with LA-ICP-MS zircon analyses with a NIST glass reference material. Res. Geol. 58, 101–123.
- Osborn, E.F., 1959. Role of oxygen pressure in the crystallization and differentiation of basaltic magma. Am. J. Science 257, 609–647.
- Paces, J.B., Miller, J.D., 1993. Precise U-Pb ages of Duluth Complex and related mafic intrusions, northeastern Minnesota: geochronological insights to physical, petrogenetic, paleomagnetic, and tectonomagmatic processes associated with the 1.1 Ga Midcontinent Rift System. J. Geophys. Res. 98, 13997–14013.
- Palenik, C.S., Nasdala, L., Ewing, R.C., 2003. Radiation damage in zircon. Am. Min. 88, 770–781
- Pasteris, J.D., 1985. Relationships between temperature and oxygen fugacity among Fe-Ti oxides in two regions of the Duluth complex. Can. Min. 23, 111–127.
- Popa, K., Prieur, D., Manara, D., Naji, M., Vigier, J.-F., Martin, P.M., Dieste, B.O., Scheinost, A.C., Prüβmann, T., Vitova, T., Raison, P.E., Somers, J., Konings, R.J.M., 2016. Further insights into the chemistry of the Bi–U–O system. Dalton Trans. 45, 7847–7855.
- Rehr, J.J., Kas, J.J., Prange, M.P., Sorini, A.P., Takimoto, Y., Vila, F., 2009. Ab initio theory and calculations of X-ray spectra. Comptes. Rendus. Phys. 10, 548–559.
- Reischmann, T., 1995. Precise U/Pb age determination with baddeleyite (Zr02), a case study from the Phalaborwa Igneous Complex, South Africa. S. Afr. J. Geol. 98.
- Richards, J.P., 2015. The oxidation state, and sulfur and Cu contents of arc magmas: implications for metallogeny. Lithos 233, 27–45.
- Rodionov, N.V., Belyatsky, B.V., Antonov, A.V., Kapitonov, I.N., Sergeev, S.A., 2012. Comparative in-situ U-Th-Pb geochronology and trace element composition of baddeleyite and low-U zircon from carbonatites of the Palaeozoic Kovdor alkaline-ultramafic complex, Kola Peninsula, Russia. Gond. Res. 21, 728-744.
- Schmitz, M.D., Bowring, S.A., 2001. U-Pb zircon and titanite systematics of the Fish Canyon Tuff: an assessment of high-precision U-Pb geochronology and its application to young volcanic rocks. Geochim. Cosmochim. Acta 65, 2571–2587.
- Schoene, B., Bowring, S.A., 2006. U-Pb systematics of the McClure Mountain syenite: thermochronological constraints on the age of the 40Ar/39Ar standard MMhb. Contrib. Min. Petrol. 151, 615–630.
- Schreiber, H.D., 1987. An electrochemical series of redox couples in silicate melts: a review and applications to geochemistry. J. Geophys. Res. 92, 9225.
- Shannon, R.D., 1976. Revised effective ionic radii and systematic studies of interatomic distances in halides and chalcogenides. Acta Cryst. A 32, 751–767.
- Smythe, D.J., Brenan, J.M., 2016. Magmatic oxygen fugacity estimated using zircon-melt partitioning of cerium. EPSL 453, 260–266.
- Sutton, S.R., Karner, J., Papike, J., Delaney, J.S., Shearer, C., Newville, M., Eng, P., Rivers, M., Dyar, M.D., 2005. Vanadium K edge XANES of synthetic and natural basaltic glasses and application to microscale oxygen barometry. Geochim. Cosmochim. Acta 69, 2333–2348.
- Sutton, S.R., Lanzirotti, A., Newville, M., Rivers, M.L., Eng, P., Lefticariu, L., 2017.
 Spatially resolved elemental analysis, spectroscopy and diffraction at the GSECARS sector at the advanced photon source. J. Environ. Oual. 46, 1158–1165.
- Tanaka, K., Takahashi, Y., 2019. Application of My-edge XANES to determination of U oxidation state in zircon. Geochem. J. 53, 329–331.
- Thomson, S.N., Gehrels, G.E., Ruiz, J., Buchwaldt, R., 2012. Routine low-damage apatite U-Pb dating using laser ablation-multicollector-ICPMS: apatite LA-MC-ICPMS U-PB dating. Geochem. Geophys. Geosyst. 13.
- Tiepolo, M., Oberti, R., Vannucci, R., 2002. Trace-element incorporation in titanite: constraints from experimentally determined solid/liquid partition coefficients. Chem. Geol. 191, 105–119.
- Tissot, F.L.H., Ibanez-Mejia, M., Boehnke, P., Dauphas, N., McGee, D., Grove, T.L., Harrison, T.M., 2019. 238U/235U measurement in single-zircon crystals: implications for the Hadean environment, magmatic differentiation and geochronology. J. Anal. At. Spectrom. 34, 2035–2052.
- Tissot, F.L.H., Ibañez-Mejia, M., 2021. Unlocking the single-crystal record of heavy stable isotopes. Elements 17, 389–394.
- Trail, D., Watson, E.B., Tailby, N.D., 2011. The oxidation state of Hadean magmas and implications for early Earth's atmosphere. Nature 480, 79–82.
- Trail, D., Bruce, W.E., Tailby, N.D., 2012. Ce and Eu anomalies in zircon as proxies for the oxidation state of magmas. Geochim. Cosmochim. Acta 97, 70–87.
- Trail, D., Tailby, N.D., Lanzirotti, A., Newville, M., Thomas, J.B., Watson, E.B., 2015.
 Redox evolution of silicic magmas: insights from XANES measurements of Ce valence in Bishop Tuff zircons. Chem. Geol. 402, 77–88.
- Underwood, S.J., Feeley, T.C., Clynne, M.A., 2012. Hydrogen isotope investigation of amphibole and biotite phenocrysts in silicic magmas erupted at Lassen Volcanic Center, California. J. Volcan. Geotherm. Res. 227–228, 32–49.
- Vance, E.R., Mackey, D.J., 1974. Optical study of U5+ in zircon. J. Phys. C Solid State Phys. 7, 1898–1908.
- Wiedenbeck, M., Allé, P., Corfu, F., Griffin, W.L., Meier, M., Oberli, F., Quadt, A.V., Roddick, J.C., Spiegel, W., 1995. Three natural zircon standards for U-TH-PB, LU-HF, trace elements and REE analyses. Geostand. Geoanalyt. Res 19, 1–23.
- Wiedenbeck, M., Hanchar, J.M., Peck, W.H., Sylvester, P., Valley, J., Whitehouse, M., Kronz, A., Morishita, Y., Nasdala, L., Fiebig, J., Franchi, I., Girard, J.-P., Greenwood, R.C., Hinton, R., Kita, N., Mason, P.R.D., Norman, M., Ogasawara, M., Piccoli, P.M., Rhede, D., Satoh, H., Schulz-Dobrick, B., Skår, O., Mj, S., Terada, K., Tindle, A., Togashi, S., Vennemann, T., Xie, Q., Zheng, Y.-F., 2004. Further Characterisation of the 91500 Zircon Crystal. Geostand. Geoanalyt. Res 28, 9–39.

- Xirouchakis, D., Lindsley, D.H., 1998. Equilibria among titanite, hedenbergite, fayalite, quartz, ilmenite, and magnetite; experiments and internally consistent thermodynamic data for titanite. Am. Min. 83, 712–725.

 Yamamoto, K., Asanuma, H., Takahashi, H., Hirata, T., 2021. In situ isotopic analysis of
- Yamamoto, K., Asanuma, H., Takahashi, H., Hirata, T., 2021. In situ isotopic analysis of uranium using a new data acquisition protocol for 10–13 ohm Faraday amplifiers. J. Anal. At. Spectrom 36, 668–675.
- Zhang, M., Salje, E.K.H., Ewing, R.C., 2003. Oxidation state of uranium in metamict and annealed zircon: near-infrared spectroscopic quantitative analysis. J. Phys.: Condens Matter 15, 3445–3470.
- Zou, X., Qin, K., Han, X., Li, G., Evans, N.J., Li, Z., Yang, W., 2019. Insight into zircon REE oxybarometers: a lattice strain model perspective. EPSL 506, 87–96.